Mapping of the podocin proximity-dependent proteome reveals novels components of the kidney podocyte foot process

Gary F. Gerlach, Zachary H. Imseis, Shamus L. Cooper, Anabella N. Santos, and Lori L. O'Brien

Affiliations:
Department of Cell Biology and Physiology, University of North Carolina at Chapel Hill, Chapel Hill, NC 27599

Corresponding author:
Lori L. O'Brien
lori_obrien@med.unc.edu

Abstract

The unique architecture of glomerular podocytes is integral to kidney filtration. Interdigitating foot processes extend from the podocyte cell body, wrap around fenestrated capillaries, and form specialized junctional complexes termed slit diaphragms to create a molecular sieve. However, the full complement of proteins which maintain foot process integrity, and how this localized proteome changes with disease, remains to be elucidated. Proximity-dependent biotin identification (BioID) enables the identification of spatially localized proteomes. To this end, we developed a novel *in vivo* BioID knock-in mouse model. We utilized the slit diaphragm protein podocin (*Nphs2*) to create a podocin-BioID fusion. Podocin-BioID localizes to the slit diaphragm and biotin injection leads to podocyte-specific protein biotinylation. We isolated the biotinylated proteins and performed mass spectrometry to identify proximal interactors. Gene ontology analysis of 54 proteins specifically enriched in our podocin-BioID sample revealed 'cell junctions', 'actin binding', and 'cytoskeleton organization' as top terms. Known foot process components were identified and we further uncovered two novel proteins: the tricellular junctional protein Ildr2 and the CDC42 and N-WASP interactor Fnbp1l. We confirmed Ildr2 and Fnbp1l are expressed by podocytes and partially colocalize with podocin. Finally, we investigated how this proteome changes with age and uncovered a significant increase in Ildr2. This was confirmed by immunofluorescence on human kidney samples and suggests altered junctional composition may preserve podocyte integrity. Together, these assays have led to new insights into podocyte biology and supports the efficacy of utilizing BioID *in vivo* to interrogate spatially localized proteomes in health, aging, and disease.

Introduction

Kidneys perform vital functions as they filter waste and toxins from the blood and regulate body fluid homeostasis. The simplest functional unit of the kidney is the nephron, composed of a blood filter termed the glomerulus connected to a segmented tubule. The glomerulus operates as a 'molecular sieve', filtering blood and inhibiting passage of large macromolecules and red blood cells into the nephron tubule. The glomerulus relies on specialized epithelial cells called podocytes, named for their unique cellular morphology with long extruding projections, termed foot processes. Podocyte foot processes wrap around a tuft of fenestrated endothelial capillaries leaving small gaps, or slits, between them. Podocytes undergo morphological changes to their junctional architecture during development to form a specialized barrier between foot processes termed a slit diaphragm.[1–3] The slit diaphragm executes multiple functions including macromolecular filtering in collaboration with the underlying glomerular basement membrane, connection to the actin cytoskeleton to maintain foot process architecture, and signaling that regulates podocyte integrity. The slit diaphragm is distinct from other junctional complexes as it integrates unique structural components as well as components of adherens and tight junctions [4–8]. Nearly 50 years ago, a zipper-like model for the slit diaphragm was proposed, wherein proteins from neighboring foot processes partially cross the intervening intercellular space and overlap, forming the dense protein-rich slit diaphragm structure eloquently visualized by electron microscopy (EM).[9,10] More recent block-face scanning electron microscopy has revealed a 'ridge-like prominence' architecture to podocyte foot processes, formed on the basal surface of the primary foot process.[2,11] These investigations underscore the continued advancement in our understanding of podocyte structure and function.

When podocytes undergo stress or injury above a threshold, they initiate a response that leads to foot process effacement, loss of slit diaphragms, and proteinuria. Loss of podocyte integrity, observed as effacement, is associated with proteinuric kidney disease[12–14]. This pathology has been described in both acquired and hereditary forms of glomerular disorders or podocytopathies.[15] Podocytopathies are a class of kidney diseases in which direct or indirect podocyte injury drives proteinuria or nephrotic syndrome and can ultimately lead to end-stage renal disease (ESRD). Genetic studies have previously identified mutations in numerous podocyte foot process components such as Membrane associated guanylate kinase WW and PDZ Domain Containing 2 (MAGI2)[16], CD2-associated protein (CD2AP)[17,18], nephrin (NPHS1)[6,19], and podocin (NPHS2)[7,20] as causal for nephrotic disease. Additionally, diseases such as diabetes and autoimmune disorders can lead to podocyte injury[21]. While the downstream result is effacement and loss of slit diaphragms, we know little about the temporal changes occurring specifically within the foot process and locally at the slit diaphragm.

The identification of slit diaphragm protein complexes with immunoprecipitation followed by mass spectrometry (MS) has uncovered important localized interactions[22,23]. However, the efficiency of these immunoprecipitations is often hindered by harsh conditions required to extract membrane proteins, which can eliminate weaker binding interactions, or by antibodies that may disrupt interactions. Additionally, transient interactions may be missed in such experiments. Podocin is known to localize to the slit diaphragm and interacts with both nephrin, Neph1, and Cd2ap.[24–27] Podocin is a member of the stomatin family, containing a central hinge region that integrates into the membrane of the foot process with cytoplasmic N and C termini.[28] Previous studies demonstrated podocin's role in the development of the multiprotein-lipid super complex of the slit diaphragm.[27] Podocin's ability to oligomerize and act as a protein scaffold at slit diaphragms ideally positions it for use as a bait protein in proteomic studies.

The discovery and engineering of a promiscuous prokaryotic biotin ligase by Roux and colleagues and concomitant blossoming of –omics technologies in the last decade have laid the groundwork to uncover spatially localized proteomes.[29,30] Proximity-dependent biotin identification,

or BioID, utilizes a mutated prokaryotic biotin ligase fused to a bait protein of interest to covalently attach biotin to proteins within the vicinity of a bait protein. The radius of biotinylation can range from ~10nm to 25nm, dependent on the size of the linker between the bait and the biotin ligase, allowing for the biotinylation of both direct and indirect interactors.[29,30] The BioID system requires exogenous addition of biotin for the ligase to covalently biotinylate a proximally located protein, giving the BioID system spatiotemporal control of protein tagging. Additionally, the biotin labels are stable and can withstand harsh isolation conditions, allowing the capture of transient interactors and membrane proteins, respectively. The BioID system has provided plentiful *in vitro* reports from cell culture models that highlight the power of the system and its ability to discover novel components of even well-documented cellular machinery such as the centrosome and cilium.[31,32] There have been limited *in vivo* reports of BioID, but it has been used successfully in vertebrates such as zebrafish and mice to identify endogenous interactomes.[32–34] To the best of our knowledge, this approach has not been employed in the mammalian kidney.

Here, we utilized gene editing to introduce a smaller, more efficient promiscuous biotin ligase (BioID2) into the endogenous murine *Nphs2* locus to create a fusion protein, hereafter referred to as podocin-BioID (*Nphs2*^{BioID2}). Our podocin-BioID model offers the capacity to uncover proteins that localize to the region of the podocyte foot process within the vicinity of podocin in an *in vivo* mammalian system. We were able to identify novel podocyte foot process proteins and furthermore how this proteome changes with age, highlighting the utility of our model for uncovering new interactors as well as disease-associated changes.

Results

Generation of the *Nphs2*^{BioID2} knock-in mouse model

To generate our mouse model, we utilized CRISPR/Cas9 gene editing in combination with homology-directed repair to knock-in the HA-tagged, mutated *A. aeolicus* biotin ligase (BioID2) in frame at the *Nphs2* locus[30]. A single guide RNA (sgRNA) was used to target the stop codon within the eighth exon of *Nphs2* to create the fusion. A 13x Glycine/Serine(G/S) flexible linker region was included between *Nphs2* and the ligase to provide up to a 25nm reach (Figure 1A)[30]. C57BL/6J zygotes were injected and after screening the resulting animals for a single knock-in with the correct sequence, several founders were identified. A single male founder was utilized for subsequent breeding and expansion of the *Nphs2*^{BioID2} line. Genotyping E18.5-P0 pups from incrosses of *Nphs2*$^{BioID2/+}$ animals identified wildtype, heterozygous, and homozygous offspring at approximately anticipated Mendelian ratios of 29%, 52%, and 19%, respectively (n=73, Figure 1B,C). However, we were typically unable to recover homozygous *Nphs2*$^{BioID2/BioID2}$ pups after 1-week of birth. Overall, the gross morphology of homozygous pups and kidneys appeared normal at P0 and we were unable to determine the specific cause of their death. Due to the early homozygous death, all subsequent experiments for proteomic profiling were performed on heterozygous *Nphs2*$^{BioID2/+}$ animals. To test the function of the podocin-ID fusion and determine if the ligase was able to biotinylate podocyte proteins, we administered 5 mg/kg biotin for 7 consecutive days to 8-10 week old *Nphs2*$^{BioID2/+}$ and wild type control mice, a dosage utilized in previous protocols for *in vivo* BioID experiments.[34] Following 1 week of subcutaneous biotin injections, kidneys harvested from *Nphs2*$^{BioID2/+}$ mice displayed a pronounced streptavidin signal within glomeruli and specifically podocytes marked by Wt1-positive nuclei (Figure 1D). We occasionally detected streptavidin-positive signal within the tubules which either represents background staining or uptake of free biotin, as controls also displayed this non-glomerular signal pattern. Finally, probing for the HA tag contained within the podocin-BioID fusion shows that the HA signal overlaps with the streptavidin signal, confirming the fusion protein is being specifically translated in podocytes and that the biotin ligase is functional (Figure 1D).

Podocin-BioID kidneys display normal nephron morphology and the fusion localizes to the slit diaphragm

We further wanted to confirm that the kidneys of animals expressing the podocin-BioID fusion did not display any significant phenotypic differences, most specifically to the nephron. If the fusion protein was not localizing or functioning properly, the animals may display phenotypes associated with *Nphs2* knockout animals such as enlarged glomeruli, vacuolated podocytes, and mesangial expansion.[35] Additionally, dilated tubules may indicate abnormal nephron function. Immunostaining kidney sections of wild type, heterozygous, and homozygous animals at E18.5 revealed no qualitative differences in glomerular size or proximal tubule dilation (Figure 2A). This further supports that mislocalization or abnormal function of podocin-ID in podocytes is not the likely cause of death in the homozygous animals. Immunofluorescence staining showed a significant overlap between the HA signal and signal from a podocin-specific antibody, supporting that the fusion protein is localizing properly in heterozygous animals and that it is being expressed at similar levels in the homozygous animals (Figure 2A). Importantly, we did not observe the HA antibody signal anywhere else besides the glomerulus.

Additionally, we wanted to confirm that the podocin-BioID protein was localizing to the slit diaphragm where podocin is known to interact with other slit diaphragm proteins and play a functional role.[24–27,35] We utilized immunogold labeling in combination with transmission electron microscopy (TEM) to examine the subcellular localization of the podocin-BioID protein (Figure 2B, B'). *Nphs2*$^{BioID2+}$ kidney sections were stained with an anti-HA antibody followed by a colloidal gold-AffiniPure secondary. Punctate gold signals were observed near electron dense regions between foot processes, the location of the slit diaphragm (Figure 2B, B' arrowheads). We observed minimal gold signal outside of this region. To confirm that this is the site of normal podocin localization in our control animals, wildtype littermates were probed with a podocin antibody and also showed localization of punctate gold signal near the electron dense region of the slit diaphragm (Figure 2 C, arrowheads).

An enrichment of biotinylated proteins is detected in lysates from *Nphs2*$^{BioID2/+}$ kidneys

To enrich our podocin-BioID protein lysates for glomeruli, we surgically isolated the cortex from each kidney of *Nphs2*$^{BioID2/+}$ animals and wildtype controls at 8-10 weeks. Isolated cortex was homogenized and lysed to obtain protein lysates from each animal. Protein lysates were applied to magnetic streptavidin coated beads to isolate the biotinylated proteins and an aliquot was removed and tested to validate the efficacy of the biotin ligase. By Western blot analysis, we identified an increase in the number of biotinylated proteins in our *Nphs2*$^{BioID2/+}$ sample versus wildtype along the full spectrum of molecular weights (Figure 3A). In contrast, few streptavidin labeled, biotinylated, proteins were visible in controls. The few biotinylated proteins observed in wildtype littermates likely represent the endogenous metabolic CoA carboxylases[36]. Due to podocin's ability to oligomerize and the heterozygous nature of the mice, we would expect that endogenous, non-tagged podocin would be biotinylated as well as podocin-BioID itself. When we probed the Western blot for podocin, we observed two bands within the *Nphs2*$^{BioID2/+}$ sample: one band at approximately 50 kDa, the predicted endogenous podocin molecular weight without the BioID2 tag (Figure 3C, denoted with an asterisk), and a second larger protein, podocin-BioID (Figure 3C, denoted with arrowhead). No bands for podocin or podocin-BioID were detected in controls, as expected. Additionally, the HA signal on the BioID2 protein was only detected in our *Nphs2*$^{BioID2/+}$ protein lysates confirming the purity and specificity of our results (Figure 3B). We went on to test if biotin could cross the placental barrier to be delivered to embryonic pups *via* injection of the pregnant dam. Pregnant dams were injected each day for one week, from E11.5-E18.5, subcutaneously with 5 mg/kg biotin. Pups were then collected at P0. We analyzed the kidney cortex and observed a strong streptavidin signal within the glomeruli of P0, *Nphs2*$^{BioID2/+}$ mice (Fig 3D, arrowheads). Contrarily, we did not observe signal in wildtype control littermate mice.

Together, these data highlight the efficacy and specificity of our podocin-BioID model which can be utilized across a spectrum of ages.

Identification of the podocyte foot process proteome by mass spectrometry profiling

Kidney cortices of three 8 to 10-week-old, sex matched mice were collected as one biological replicate, after biotin administration for 1 week. All MS analyses were run in triplicate *i.e.* 9 mice per condition, totaling 18 mice (*Nphs2*$^{BioID2/+}$ vs control littermates) per MS analysis. To representatively capture the podocyte foot process proteome, we combined the results of three separate MS analyses, representing 54 total mice (Figure 4). Significant sex differences were not apparent in our studies (Supplemental Tables II-IV). From our proteomics analysis 11 proteins were found across all three MS analyses to have an averaged Log_2 fold change $\geq$ 2.5. Many of these top proteins including podocin, Kirrel, Tjp1, Pard3, Magi2, Dnd, and Synpo are documented to localize to the slit diaphragm.[37] Yet others including an Immunoglobulin like domain containing receptor 2 (Ildr2) and a Formin binding protein 1 like (Fnbp1l, also known as Toca1) were, until now, unreported components of the podocyte foot process/slit diaphragm. Additionally, 6 proteins were identified across two MS analyses as significantly unregulated with an average Log_2 fold change $\geq$1.75. These include documented slit diaphragm components Tjp2 and Cd2ap (Figure 4A). All top 17 proteins had a stringent Log_2 fold change $\geq$ 1.75. Tables listing the significant foot process proteins identified from each MS analysis are reported in Supplemental Tables II – IV. To add support to our relative Log_2 fold cut off, we assayed an immunoglobulin superfamily adhesion molecule, Jam1/F11r,[38] with an observed Log_2 fold expression change of 0.7 (Supplemental Table II). We identified Jam1 expression in cells of the proximal convoluted tubule, abutting the glomerulus, (Supplemental Figure 1) but not within the glomerulus. Potentially, non-glomerular cortex proteins that are biotinylated are also isolated although these appear minimal in our findings. However, this helped establish a relative fold-cutoff for which we start to identify non-podocyte proteins.

To surmount a complete list of podocyte foot process proteins we established a Log_2 fold change cut off at 1.2 across all three mass spec analyses, and excluded histone, ribosome, and mitochondrial proteins to arrive at a catalog of 54 proteins (Supplemental Table V). Graphically depicting the compiled proteome in a volcano plot with the total ~1400 proteins identified and cataloging proteins with a Log_2 fold change $\geq$ 1.75 and *p*-value $\leq$ 0.05 in green, proteins found to have a *p*-value $\leq$ 0.05 in blue and proteins not found to be significant in grey (Figure 4B, Supplemental Table V). The blue dotted line represents a $-Log_{10}$ (*p*-value$\leq$ 0.05) (Figure 4B). All significantly identified proteins ($p \leq 0.05$) had at least two unique peptides identified via MS analysis. The most highly detected and significant proteins from our proteomic profiling, clustering with documented slit diaphragm components, are found in the right scatter of the volcano plot, depicted with green dots (Figure 4B, Supplemental Table V).

To interrogate our proteomic findings further, the top 54 podocyte foot process proteins were utilized for *in silico* analyses. We input Supplemental Table V into *Qiagen Ingenuity Pathway Analysis (IPA)* and performed a variant effect analysis to compute a proposed interactome based on published literature (Figure 4C). The representative web of interactions from IPA was color coded based on the number of MS analyses each protein appeared in, one (yellow), two (light green), and three (dark green) (Figure 4C). Two novel foot process proteins were identified by IPA, Ildr2 and Fnbp1l, to be involved in the interactome with connections to Afadin and actin, respectively (Figure 4C). We added two dotted magenta lines for Ildr2 and Fnbp1l potential interactions with podocin (Figure 4C). Unshaded proteins and dashed lines are predicted interactors/interactions from IPA. Our IPA proposed network includes 26 of our 54 input foot process proteins. The IPA interactome identifies three main nodes, *i.e.* junctions, cytoskeleton, and signaling (Figure 4D). We highlighted the respective proteins that contribute to each node for

junctions (cyan), cytoskeleton (magenta), and signaling (orange) (Figure 4D). We next input these 54 proteins into the *Database for Annotation, Visualization, and Integrated Discovery (DAVID)* to identify the gene ontogeny (GO) terms that are most highly enriched across our foot process proteome. DAVID analysis identified cytoskeleton protein binding, cell-cell junctions, and actin filament-based processes as the top molecular function, cellular component, and biological processes GO terms, respectively (Figure 5A). Additionally, DAVID and IPA overlap in their representation of junctional signaling and actin binding as top GO terms and canonical pathway respectively. Taken together, these findings align with the major functional role roles of podocin and other foot process/slit diaphragm components.

To further decipher the contributions of our top 54 podocyte foot process proteins to junctions and cell-cell contacts we cataloged the protein domains represented within each protein. We utilized binary counting for the presence and absence of a domain. We did not account for the number of same/similar domain(s), *i.e.* SH2/3, within a protein. We identified 7 top protein domains within the catalog of the podocyte foot process proteome that included SH, PDZ, FERM and Ig-like domains among others (Figure 5B). All of these top protein domains align with the nodes of the podocyte foot process proteome*, i.e.* junctions, cytoskeleton, and signaling.

Ildr2 and Fnbp1l are expressed by podocytes and co-localize with podocin

Our proteomic analyses uncovered several proteins which have not been previously described to localized to the podocyte foot process or have podocyte-specific functions. We therefore wanted to validate their expression in podocytes and any colocalization with podocin. We utilized immunofluorescence on kidney sections to visualize the location of three proteins in particular: Myozap, Fnbp1l, and Ildr2. First, a known slit diaphragm and foot process component which was identified in our proteomics, Pard3, was assessed for its colocalization with podocin. Pard3 both exhibited positive staining in the glomerulus and overlapped with the HA signal of podocin-BioID (Figure 6A). Pard3 positive staining is also found in the adjacent tubule cells where it helps maintain epithelial integrity (Figure 5A).[39] Myozap regulates cardiac function through Rho-dependent activity and interacts with junctional proteins such as ZO-1[40]. It was identified across two of the three MS analyses (Figure 4A) and therefore we decided to investigate its localization. Utilizing an antibody against a synthetic human MYOZAP peptide,[41] we identified strong signal of Myozap in the kidney endothelium, both in the glomerular capillaries and outside of glomerular structures (Supplemental Figure 2). Myozap exhibits some degree of overlap with podocin, however, the majority of Myozap protein detection does not colocalize with podocin, suggestive of additional roles outside of podocytes (Supplemental Figure 2).

We identified Fnbp1l, a documented junctional and actin organizing protein,[42, 43] across all three MS analyses with a Log_2 fold change > 4 (Figure 4). Fnbp1l has been identified in human and mouse podocytes from single cell RNA-seq analysis and linked to podocyte cytoskeleton dynamics *in vitro*, although it has not been documented to colocalize with the slit diaphragm or foot process-associated proteins.[44,45] We found that Fnbp1l co-localizes with podocin in continuous stretches within glomeruli observed as a white signal from the Fnbp1l (magenta) and podocin (green) overlap (Figure 6C). *In situ* hybridization confirms the glomerular expression of *Fnpb1l* (Figure 7C' arrowhead), similar to *Nphs2* (Figure 7A), in addition to a tubular expression pattern at postnatal day 2 (P2).

Ildr2, a member of the B7 superfamily of immunoglobulins, is found highly enriched in the podocyte foot process proteome across all MS profiles with an average Log_2 fold change of 4.9 (Figure 4). Ildr2 is a member of the angulin family and localizes to tricellular junctions of *in vitro* cultured epithelial cells[46]. In the kidney, Ildr2 exhibited a punctate staining pattern that colocalized with podocin in adult mouse glomeruli, reminiscent of the punctate and restricted pattern of tricellular junction staining observed *in vitro* (Figure 6B, 6D arrowheads)[46]. In the z dimension we observe overlap of Ildr2 (magenta) with podocin (green) as white punctate foci denoted by

arrowheads (Figure 6D). We further validated *Ildr2* expression within glomeruli via *in situ* hybridization. Ildr2 expression is found in glomeruli (Figure 7B' arrowhead) and tubule cells of the kidney (Figure 7B' arrow) in P2 mice. We went on to verify Ildr2 localization within early renal vesicles, comma, and S-shaped bodies of developing nephrons at E15.5 (Figure 8B, Supplemental Figure 3). Ildr2 is more membranous and contiguous yet with some punctate detection in early embryonic stages (E15.5) both within podocytes and cells of the developing nephron tubule (Figure 8B). Collectively these studies provide evidence that Ildr2 and Fnbp1l are novel podocyte foot process and potentially slit diaphragm components that likely play roles in helping to maintain podocyte architecture.

Ildr2 protein levels increase in both mouse and human glomeruli

To determine whether our podocin-BioID model can detect changes to the localized proteome in aging, we performed proteomics on 108-week-old male *Nphs2*$^{BioID2/+}$ mice and compared the results to our 8-10 week old *Nphs2*$^{BioID2/+}$ male mice to assess any changes (Figure 8A). We identified significant increases in Tjp2 and Pkp4 and the largest change (2.76-fold) in Ildr2 (Figure 8A). We were unable to detect any significant decrease in proteins at $p \leq 0.05$, although Fnbp1l and Tns2 showed a decreasing trend. We observed minimal change in podocin when comparing the two age groups (Figure 8A). To assess the human relevance of our findings, we assayed ILDR2 immunofluorescent staining in young (age ~30 years) and aged (91-year-old) human kidney sections. ILDR2 displayed a similar punctate staining pattern in young human glomeruli. In correlation with our findings from the mouse, we found an increase in ILDR2 staining in the aged glomeruli. Interestingly, the expression pattern no longer displays a punctate pattern but rather a more diffuse membranous staining pattern (Figure 8C). We quantified the corrected total glomerular florescence (CTGF) by selecting the glomerulus as a region of interest (gROI) then quantifying total florescence intensity and subtracting out the mean background florescence for the glomerular area, *i.e.* total gROI florescence – (glomerular area x mean background florescence) = CTGF, (Figure 9A). We confirmed a significant ($p \leq 0.007$) increase in Ildr2 in aged human glomeruli compared to young human kidney tissue (Figure 9A).

Discussion

Podocytes are extraordinary epithelial cells of the kidney that intertwine their foot process extensions to establish a cellular junction, the slit diaphragm, that is distinct from other cellular junctions in the human body. The slit diaphragm was identified more than five decades ago as an electron dense region between two podocyte foot processes, visualized beautifully by EM.[47,48] Many proteins that compose the slit diaphragm when mutated are associated with nephrotic diseases, including nephrin, podocin, Magi2, and Cd2ap.[49] Loss of podocyte integrity is one of the most common clinical observations in kidney disease. End stage renal disease being a top 10 cause of death in the US necessitates the need to identify novel components of the slit diaphragm, and how the slit diaphragm changes with disease, for the development of new therapeutic options and biomarkers of disease severity.

We utilized a new *in vivo* biochemical tool to interrogate the proteome of the podocyte foot process *via* knock-in of a BioID moiety, generating our podocin-BioID model. The sensitivity and advantage of BioID is that it allows for weak and transient interactions to be identified, in addition to withstanding harsh isolation conditions.[6] Further, the biotin-streptavidin bond is one of the strongest known non-covalent interactions, enhancing the isolation of biotinylated proteins via streptavidin-coated magnetic bead. We validated our model recapitulates normal podocin localization by TEM and showing podocin-BioID localizes normally to the slit diaphragm. Activity of the biotin ligase was confirmed through probing kidney sections and lysates with streptavidin and finding an enrichment of biotinylated proteins. Our proteomics profiling identified more than 50

395 candidate molecules with significant enrichment in the podocyte foot process, $Log_2 \geq 1.2$. Within
396 this dataset we were able to identify novel candidates not found in previous investigations of the
397 slit diaphragm proteome[22,23]. Additionally, we were able to identify changes to the localized
398 proteome that occur with aging. It would be interesting to compare the proteome across additional
399 stages such as during development. Podocytes begin as a columnar epithelium with only tight and
400 adherens junctions which remodel and later mature to form the specialized slit diaphragm
401 complex.[16] With the ability of biotin to cross the placental barrier, the proteome could be compared
402 from development to maturity to identify changes that may help inform how these specialized
403 junctions are formed.

404 The proteomics analysis revealed potential nuances of the podocyte foot process that are
405 still under investigation. We identified 11 proteins that repeated over all three MS profiles.
406 However, there were more than 30 proteins that only surfaced in a single MS analysis and split
407 across the three MS analyses. While this may be due to experimental variability, such as in the
408 isolation of proteins, this may also highlight some differences in biological activity in the foot
409 process. The dynamics, variability, and protein turnover in the podocyte slit diaphragm is relatively
410 unknown. Pointing to the relative variability of one documented component, Synaptopodin (Synpo),
411 across the three MS analyses the respective Log_2 fold changes were observed at 1.0, 2.9, and 4.8
412 which indicates potential protein turn over, variability in the slit diaphragm components, or potential
413 variability from MS to MS. Further still, a second documented slit diaphragm protein, Cd2ap, was
414 only identified in two of the MS profiles. These cofounding issues made a single MS analysis a
415 limited view, or snapshot, of the proteins present within the podocyte foot process. By combining
416 three separate MS analysis we have uncovered a more complete profile of the podocyte foot
417 process and slit diaphragm. Many of the top candidates identified in the podocyte foot process
418 proteome are well documented slit diaphragm components including Kirrel, Nphs2, Par3, Magi1/2,
419 Tjp1/2/3, Dnd, Synpo, and Cd2ap. Furthermore, our *in silico* analysis utilizing DAVID highlights
420 anticipated GO terms, including actin binding, cell-cell junctions, adherens junctions, and
421 cytoskeleton organization that align with podocyte function. We conclude the podocin-BioID model
422 provides a spatial specific approach to identify proteins that are notoriously difficult to isolate.

423 We cannot rule out biotin delivery and metabolism may limit some proteins from being
424 detected. One report depicts a time lapse of biotin administration *in vivo* with positive streptavidin
425 enrichment for as long as 18-hour after biotin administration.[50,51] However, biotin requires an
426 accessible primary amine within a peptide to biotinylate. Proteins with little open structure or a
427 limited number of lysine residues could be missed by the labeling strategy. The possibility that
428 proteins were missed is brought to light by the inability to identify nephrin (*Nphs1*) across any of
429 the mass spec analyses run. One rational for the inability to identify nephrin, a known slit
430 diaphragm molecule that has been shown to interact with podocin, posits that its C-terminal
431 domain is only minimally assessable to podocin, while the remaining majority of the 180 kDa
432 protein is spanning the extracellular space of the slit diaphragm.[27] Therefore, while there are
433 significant advantages to the BioID system over traditional immunoprecipitations followed by MS, it
434 is also subject to missing important interactions.

435 One of the novel foot process candidates we identified, Fnbp1l, has multiple roles in
436 microtubule binding, cell polarity, motility, actin organization, junctional localization and
437 signaling.[42,43] Based on these roles, we hypothesize that Fnbp1l similarly helps maintain the slit
438 diaphragm and foot process integrity through associations with the actin cytoskeleton and links to
439 the slit diaphragm. Single cell RNA-seq analyses have previously found *Fnbp1l* expression in
440 human[44] and mouse podocytes and tubule cells.[45] From the Kidney Interactive Transcriptomics
441 (KIT), *Fnbp1l* is most highly expressed in podocytes compared to the tubule cells of the human
442 kidney.[52] Further, *Fnbp1l* is also expressed in the zebrafish pronephros[53] with a similar pattern to
443 other zebrafish tight junction proteins such as ZO-1/2[54], however the specific expression of *Fnbp1l*

within the zebrafish podocytes remains unknown. With the conservation of *Fnbpl1* expression in the renal system across vertebrates, it likely plays an important role in helping maintain epithelial integrity in the various cells of the nephron, including podocytes.

Ildr2 was identified in the podocyte foot process/slit diaphragm proteome across all three MS profiles with a Log_2 fold change $\geq$ 4.5 and a *p*-value $\leq$ 0.007. Ildr2 belongs to the B7/CD28 family of proteins, encompassed by the Ig superfamily (IgSF), with pivotal roles in immunomodulation and maintenance of peripheral self-tolerance.[55] Ildr2 evinces immunomodulatory activity, wherein administration of Ildr2 as a fusion protein (ILDR2-Fc) rebalances immune homeostasis, which leads to an amelioration of autoimmune disease states in mouse models of rheumatoid arthritis, type I diabetes, and relapsing-remitting multiple sclerosis.[55-56,57] Recently, an Ildr2 blocking antibody , BAY 1905254, was generated to block the immunosuppressive activity of Ildr2 for cancer immunotherapy.[57] BAY 1905254 promotes T-cell activation *in vitro* and enhances antigen-specific T-cell proliferation and cytotoxicity *in vivo*, and is currently in phase I clinical trials.[57] Ildr2 presents an unexplored niche in podocyte biology centered around the function of podocytes in immune cell modulation. Yet, the ability for immune cells such as T-cells to interreact with podocytes is challenged by the podocyte cellular environment and the GBM. Therefore, whether Ildr2 could play an immune related role in podocytes remains tentative.

Ildr2/ILDR2 is found to be specifically expressed in mouse and human podocytes from publicly available databases including KIT.[44,58] *Ildr2* was also identified as a Wt1 transcriptional target in podocytes by ChIP-seq.[59] In early embryonic and postnatal mouse kidneys, *Ildr2/*Ildr2 is expressed and localized to tubule cells and podocytes. However, in the adult kidney Ildr2 localization becomes restricted to podocytes. At the timepoints of podocyte development, we observe a more membranous and contiguous pattern of Ildr2 in comma and s-shaped bodies, with some foci of heightened detection. In mature glomeruli, Ildr2 is restricted to punctate foci that colocalize with podocin. Ildr2 has been identified at the site of tricellular tight junctions (tTJ) in murine retinal pigment epithelium and *in vitro* within EpH4, a mouse mammary gland cell line.[46,56] Additionally, Ildr2 has recently been identified to interact with Afadin in human embryonic kidney cells (HEK293).[60] Afadin is also reported to localize to the site of specialized tricellular junctions and mediate mechanotransduction.[61] The role of mechanical strain present from the underlying fluid flow sheer stress on these specialized tTjs and recruitment of specific proteins to these domains remains unresolved. Many proteins identified in the podocyte foot process proteome are documented junctional proteins containing classified SH, PDZ, FERM, transmembrane, EF-Hand, and Ig-like domains. Yet, Ig-like domain containing proteins were a considerably smaller population. It is intriguing to speculate that Ig-like domains or a combination of PDZ, SH, and Ig-like domain aids in the recruitment of specific proteins to specialized junctions such as tTJs and the slit diaphragm. Further still, the requirement of these proteins for managing stress such as from changes in fluid flow from the fenestrated endothelium and conversely the potential requirement of mechanostress for recruitment of proteins to these tTJs and slit diaphragms remains an area in need of further investigation.

In our aged podocin-BioID mice as well as our aged human kidney sample, we identified an increase in Ildr2 within podocytes. The pattern of Ildr2 is more membranous with some punctate foci in embryonic renal structures yet becomes detectable only as punctate foci as the mouse matures. Proteomic profiling of 108-week-old, aged mice identify a significant increase in Ildr2 detection. We validated Ildr2 significantly increases in aged (91 yo) human glomeruli via quantifying the corrected total glomerular florescence of young and aged human glomeruli. We further noted that in the aged human glomeruli Ildr2 is detected higher in zones where podocin is less detected and conversely where podocin is detected high Ildr2 is less abundant. Aged human glomeruli present an Ildr2 pattern that more closely resembles the mouse embryonic stage with a contiguous pattern rather than the punctate pattern of younger mice. We hypothesize that Ildr2 is a

tight junction component and increasing Ildr2 protein in aged podocytes helps maintain podocyte integrity with age. The additional increase of tight junction and desmosome associated proteins Tjp2 and Pkp4, respectively, in our aged mouse proteome further supports this hypothesis.

In this study, we developed an innovative tool for the identification of novel proteins within spatially restricted podocyte foot process/ slit diaphragm. Current efforts are now aimed at uncovering proteins differentially regulated during slit diaphragm development, aging, and in renal disease. It is crucial we uncover the changing composition of the podocyte slit diaphragm and foot process as it holds potential for new therapeutic treatment targets to either preserve or prevent the loss of podocyte integrity in kidney disease.

Methods

Genetic CRISPR/Cas9 engineering of the Nphs2 locus to append a BioID2 moiety

CRISPR/Cas9 targeting, and donor vector design were performed by UNC Chapel Hill Animal Models Core. *Benchling* software was used to identify Cas9 short guide RNAs (sgRNA) overlapping the podocin (*Nphs2*) stop codon. Guide RNAs were cloned into a T7 promoter vector followed by *in vitro* transcription and spin column purification. Functional testing was performed by transfecting a mouse embryonic fibroblast cell line with sgRNA and Cas9 protein (produced and purified by the UNC Protein Expression Core). The sgRNA target region was amplified from transfected cells and analyzed by T7 endo1 nuclease assay (New England Biolabs). sgRNA, *Nphs2*-g78B (protospacer sequence 5'-gCCATTCGCCTATAACAT-3'; lower case g indicates heterologous guanine added at 5' end of native sequence for efficient T7 *in vitro* transcription) was selected for genome editing in embryos. *Nphs2* was amplified from adult mouse kidney cDNA and cloned into the MCS-BioID2-HA plasmid (plasmid was a gift from Kyle Roux; Addgene plasmid # 74224 ; http://n2t.net/addgene:74224 ; RRID:Addgene_74224).[30] A donor vector was subsequently constructed from the *Nphs2*-BioID2-HA plasmid with the following features: (1) a 1018 bp 5' homology arm encompassing sequence immediately 5' of the *Nphs2* stop codon including 276 bp coding sequence from *Nphs2* exon 8, (2) a 267 bp in-frame Glycine/Serine-rich linker sequence, (3) a 696 bp coding sequence for the humanized biotin ligase of *A. aeolicus* with a R40G mutation in the catalytic domain (BioID2)[30], (4) HA Tag, (5) 2X Stop codon, (6) a FRT site, and (7) a 1019 bp 3' homology arm, beginning at the *Nphs2*-sgRNA cut site. The donor vector was designed to produce a final knock-in allele which would produce a fusion protein of podocin C-terminally linked to BioID2.

Embryo microinjection

C57BL/6J zygotes were microinjected with 400nM Cas9 protein, 25 ng/μl sgRNA and 20 ng/μl supercoiled double-stranded donor plasmid (Mix1), or 200 nM Cas9 protein, 12.5 ng/μl sgRNA and 10 ng/μl donor plasmid (Mix2). Injected embryos were implanted in pseudopregnant B6D2F1 recipient females. Fourteen resulting pups (9 from Mix1 and 7 from Mix2) were screened by PCR for the presence of the knock-in allele. One female (Founder #2) and one male (Founder #6) were positive for the correct single-copy knock-in allele. Founders #2 and #6 were mated to wild-type C57BL/6J animals for transmission of the knock-in allele. Both founders transmitted the correct knock-in allele to offspring. Injections, genotyping of founders, and off-site targeting analysis was performed by UNC Chapel Hill Animal Models Core.

Genotyping

A mouse tail or ear clip was taken and dissociated with Viagen DirectPCR Lysis Reagent (Mouse Tail) containing 10 *μ*g/mL proteinase K incubated at 55°C overnight and denatured at 95 °C for 10 min. PCR was run with ($T_{annealing}$ = 63.5°C), elongation for 40 sec, for 35 cycles. Primer sequences utilized for genotyping are Common Forward: 5'-CTTTTGTCCTCTCCCGGCAA-3',

542 podocin WT Reverse 5'-TGCATGTAGCCATCTTGTGACT-3', *Nphs2*^{BioID2} Reverse 5'-
543 CTGCCCTTGGTCTGTCTGTC-3'.
544
545 *Kidney cortex isolation and lysis*
546 Mice were raised, housed, and handled in accordance with IACUC protocol number 19-
547 183.0/22-136.0. 8–10-week-old mice were injected subcutaneously with 5 mg/kg biotin every day
548 for one week. We surgically isolated the cortex of the kidney to enrich for the glomerular fraction,
549 using a scalpel in cold sterile phosphate buffered saline (PBS). A single biological sample was
550 composed of the isolated kidney cortex of three same sex mice for a total of six kidney cortexes
551 per sample (2 kidneys per animal x 3 mice). The sample was then homogenized via a glass
552 Dounce homogenizer. Samples were centrifuged at 4 °C, 5000 × g for 10 minutes. Supernatant
553 was decanted and the tissue pellets snap frozen in liquid nitrogen and stored at -80 °C. Care was
554 taken to utilize sterile Eppendorf tubes that had not been autoclaved as we identified a
555 polyethylene glycol contaminant in a preliminary MS analysis that may arise from autoclaving
556 plastic utilized. Samples were removed from the freezer and allowed to equilibrate on ice for 2
557 hours. Lysis buffer (8M urea, 50mM Tris-HCl pH 7.4, 500mM NaCl, 2.5mM EDTA, 2.5mM EGTA,
558 1.5mM MgCl2, 1.5mM DTT, 0.25% NP-40, 1% SDS, 1x protease inhibitors (Roche cOmplete Mini
559 EDTA-free, Sigma)) were then added to resuspend the pellet and allowed to nutate at 4°C for one
560 hour. The protein homogenate was sonicated (3 pulses for 10 sec at 30% duty) and centrifuged
561 (4°C, 12000 rpm for 10 min). The supernatant was then removed for subsequent quantification and
562 analysis.
563
564 *Biotinylated protein capture*
565 Kidney cortex-isolated protein lysates were serial diluted and run-in triplicate on a 96-well
566 plate reader at 590nm wavelength (Synergy HT, BioTek). A standard curve of bovine serum
567 albumin (BSA) was utilized as a control. Protein concentrations of each lysate were calculated, and
568 10mg of crude protein lysate was loaded with 100μl of streptavidin-coated magnetic beads
569 (Dynabeads MyOne Streptavidin C1, Invitrogen). Samples containing beads and protein lysate
570 were rotated end over end at 4°C overnight. Supernatant was removed using a magnetic strip, and
571 the bead-captured fraction was washed once with lysis buffer. After the first wash with lysis buffer
572 containing 1% SDS and 0.25 % NP-40 diminishing amounts of detergents were utilized in
573 subsequent washes until there was no detergents remaining in the wash buffer (after 4 washes).
574 Beads were then washed 3 times in ABC solution (50mM ammonium bicarbonate, 8.0 pH) and
575 sent to UNC Chapel Hill Hooker Proteomics Core. All procedures were performed the same for our
576 aged murine cohort with the exception that 5mg of crude protein lysate was loaded onto beads.
577 After the last wash buffer step, 50µl of 50mM ammonium bicarbonate (pH 8) containing 1 µg
578 trypsin (Promega) was added to beads overnight at 37ºC with shaking. The next day, 500ng of
579 trypsin was added then incubated for an additional 3h at 37ºC with shaking. Supernatants from
580 pelleted beads were transferred, then beads were washed twice with 50ul LC/MS grade water.
581 These rinses were combined with original supernatant, then acidified to 2% formic acid. Peptides
582 were desalted with peptide desalting spin columns (Thermo Scientific) and dried via vacuum
583 centrifugation. Peptide samples were stored at -80˚C until further analysis.
584
585 *LC/MS/MS analysis*
586 Each sample was analyzed by LC-MS/MS using an Easy nLC 1200 coupled to a QExactive
587 HF (Thermo Scientific). Samples were injected onto an Easy Spray PepMap C18 column (75µm id
588 × 25cm, 2µm particle size) (Thermo Scientific) and separated over a 120 min method. The gradient
589 for separation consisted of a step gradient from 5 to 36 to 48% mobile phase B at a 250 nl/min flow
590 rate, where mobile phase A was 0.1% formic acid in water and mobile phase B consisted of 0.1%
591 formic acid in ACN. The QExactive HF was operated in data-dependent mode where the 15 most

592 intense precursors were selected for subsequent HCD fragmentation. Resolution for the precursor
593 scan (m/z 350–1700) was set to 60,000 with a target value of 3×10^6 ions, 100ms inject time.
594 MS/MS scans resolution was set to 15,000 with a target value of 1×10^5 ions, 75ms inject time.
595 The normalized collision energy was set to 27% for HCD, with an isolation window of 1.6m/z.
596 Peptide match was set to preferred, and precursors with unknown charge or a charge state of 1
597 and ≥ 8 were excluded.
598
599 *Western blot*
600 Biotinylated proteins attached to streptavidin coated bead were eluted off with excess biotin
601 [200 mM] in 200 mM Tris HCl pH: 6.8, 40% glycerol, 8 % beta mercaptoethanol, 2 % SDS, 0.04 %
602 bromophenol blue at 95°C for 30 min). Bead slurry mix was placed on a magnet and isolated
603 biotinylated lysate was collected for subsequent analysis. Protein sample fractions were removed
604 and loaded into a Novex WedgeWell gel (4-20% Tris-Glycine gradient gel, Invitrogen, XP04202),
605 and run in 25mM Tris-HCl, 190mM Glycine, 0.1% SDS, pH 8.3. Proteins were transferred from gel
606 to nitrocellulose membrane in 25mM Tris-HCl, 190mM Glycine, and 20% methanol. The membrane
607 was blocked in 3% bovine serum albumin in 1x TBST (Tris base Saline Solution (25mM Tris-HCl
608 pH 7.5, 150mM NaCl) with 0.1% Tween-20, for 1 hour at room temperature. Primary antibodies
609 (Rabbit anti-HA tag (Cell Signaling, 3724S [1:500], mouse anti-NPHS2 (Proteintech, 20384-1-AP)
610 [1:500], Rabbit anti-podocin (Invitrogen, PA5-79757) [1:500], Streptavidin-HRP (Cell Signaling,
611 3999S) [1:1000] were applied in 3% BSA+ TBST. Membrane plus primary antibodies were allowed
612 to incubate overnight at 4°C with gentle nutation. Following 3x10 min washes with TBST,
613 membranes were probed with secondary antibodies conjugated to horseradish peroxidase (HRP)
614 (donkey and rabbit -HRP [1:500] or Goat anti mouse-HRP [1:500] and incubated for one hour at
615 room temperature Membranes were developed with enhanced chemiluminescence substrate
616 (ECL) and visualized on an iBright FL1000 (Invitrogen).
617
618 *Proteomics data analysis*
619 Raw data were processed using the MaxQuant software suite (version 1.6.12.0) for
620 identification and label-free quantitation.[62] Data were searched against an Uniprot Reviewed
621 Mouse database (downloaded January 2021, containing 17,051 sequences) using the integrated
622 Andromeda search engine. A maximum of two missed tryptic cleavages was allowed. The variable
623 modification specified was oxidation of methionine, N-terminal acetylation, and phosphorylation of
624 Ser/Thr/Tyr. Label-free quantitation (LFQ) was enabled. Results were filtered to 1% FDR at the
625 unique peptide level and grouped into proteins within MaxQuant. Match between runs was
626 enabled. Data were filtered in Perseus, then imported into Argonaut for normalization, imputation
627 and statistical analysis.[63]
628 We combined three separate MS analyses and averaged the Log_2 fold changes and respective *p*-
629 values of the top 17 proteins identified across all three MS profiles. QIAGEN Ingenuity Pathway
630 Analysis (IPA) was utilized to identify putative interactomes.
631
632 *Immunofluorescence*
633 Kidneys were harvested in cold filter sterilized PBS and fixed at 4°C for 1 hr in 4%
634 paraformaldehyde (PFA) in PBS. Samples were washed twice in 1x PBS, placed in 30% sucrose
635 overnight, and subsequently embedded in OCT. Kidneys were cut in 12μm sections on a Leica
636 Cryostat CM 1850. Tissue sections were blocked in 3% donkey serum, 1% bovine serum albumin
637 (BSA), 1x PBS, 0.1 % TritonX-100 for 45 min at room temperature. Slides were incubated in
638 primary antibodies (see antibodies utilized below, Supplemental Table I) diluted in blocking buffer
639 for 1-2 hr. Slides were then rinsed 3x5 min in 1x PBST, after which they were incubated with Alexa
640 Fluor labeled secondary antibodies (Invitrogen) diluted (1:1000) in blocking buffer for 1 hr at room

temp. The slides were then rinsed 2 x 5 min with 1x PBST, 1x3–5 min with 1x PBS + 1ng/mL DAPI and mounted in ProLong Gold antifade reagent (Invitrogen).

For double labeling tissue with two antibodies both raised in rabbit we utilized a Zenon double labeling kit (Z25302, Invitrogen) with rabbit anti-Fnbp1l, rabbit anti-Ildr2, rabbit anti-podocin, and rabbit anti-HA antibodies. The weaker of the two primary rabbit antibodies, typically Ildr2 and Fnbp1l, was diluted in block solution then incubated for 90 min at room temperature. Slides were washed 3-6x with 1xPBS +0.25% Triton-X 100 and subsequently incubated for 1hr at room temperature with the appropriate Alexa Fluor-488 labeled secondary antibody diluted 1:1000 in blocking buffer. The second primary rabbit antibody was mixed at a 1:2.5 ratio with the Zenon fluorophore-647. Note the two fluorophores utilized are on opposite ends of the florescence spectrum. The slides were then fixed in 4% PFA for 5 min at room temperature. And all subsequent steps were carried out per normal immunofluorescence procedures as above. Images were acquired utilizing a Zeiss 880 confocal microscope equipped with Airyscan super-resolution and spectral imaging on Zen Microscopy Suite version 2.3 Sp1 that is part of the UNC Hooker Imaging Core. Z-stack images were acquired in 1μm steps for Ildr2 and Fnbp1l.

Immunogold electron microscopy

Mouse kidneys were fixed for 1 hour at room temperature in 4% PFA in 0.15M sodium phosphate buffer pH 7.4 (PB) or 2% PFA + 0.5% glutaraldehyde in 0.15M PB and immediately processed for LR White resin embedding. Samples were washed in 0.15M PB, 3x10 minutes and dehydrated using a Pelco BioWave Pro Microwave (Ted Pella, Inc.) as follows: at 40˚C (750 watts): 30% ethanol in water (ETOH) -1 min, 50% ETOH in water-1 min, 75% ETOH in water-1 min, and at 40˚C (450 watts): 100% ETOH-1 min, 100% ETOH-1 min, 100% ETOH-1 min. Microwave infiltration and embedment were carried out using the following schedule: 1 part 100% ETOH:2 part LR White resin-10 min at 40˚C (350 watts), 2 exchanges of 100% LR White resin for 10 min at 50˚C (350 watts). Samples were transferred to 00 gelatin capsules filled with fresh LR White resin and polymerized overnight at 55˚C; the temperature was adjusted to 60˚C for 6 hours and allowed to complete polymerization at room temperature for 72 hrs. Blocks were trimmed to the tissue and 1.0*μ*m sections were cut using Leica Ultracut UCT (Leica Microsystems, Inc.) and a Diatome diamond knife (Electron Microscopy Sciences). Sections were mounted on glass slides, stained with 1% toluidine blue O in 1% sodium borate, and regions with glomeruli were selected and trimmed.[64] Ultrathin sections (90 nm) were cut and mounted on formvar / carbon-coated 200 mesh nickel grids. Before immunostaining, the sections were hydrated by floating the grids section-side down on drops of deionized water. Sections were blocked with Aurion Goat Blocking Solution for 15 min and transferred to 15*μ*l drops of the primary antisera diluted at [1: 500] for anti-HA and [1: 250] for anti-Podocin in 0.05M TBS+0.2% BSA-Ac, pH 7.6 (Rabbit anti-HA, Cell Signaling, 37245; rabbit anti-Podocin, Invitrogen, PA5-79757). Sections were incubated overnight at 4˚C followed by 4x10 min washes in TBS/BSA-Ac to remove unbound antibody. The grids were incubated in a 12nm Colloidal gold-AffiniPure goat anti-rabbit IgG (H+L) secondary antibody (Jackson Immuno, Lot #148041) diluted at 1:50 in TBS/BSA-Ac for 2 hours at room temperature.[65] After 3 washes in TBS/BSA-Ac and 3 washes in 0.15M PB, grids were post-fixed for 10 min in 1% glutaraldehyde in 0.15M PB followed by 3 washes in deionized water. The grids were stained with 4% aqueous uranyl acetate for 5 min for additional contrast. Samples were observed using a JEOL JEM-1230 transmission electron microscope operating at 80kV (JEOL USA INC.), and images were taken using a Gatan Orius SC1000 CCD camera with Gatan Microscopy Suite version 3.10.1002.0 software (Gatan, Inc.). Sample prep and imaging was performed at the UNC Microscopy Services Laboratory, Department of Pathology and Laboratory Medicine.

In situ hybridization

Wildtype C57/Bl6J kidneys at postnatal day 2 (P2) were dissected in cold molecular grade PBS (RNAse/DNAse free) and fixed in 4% PFA for 30 min at room temperature on a rocking platform. Kidneys were washed in molecular grade PBS and placed in 30% sucrose. Kidneys were embedded in OCT and 20μm sections were cut on a cryostat (Leica CM1850). Tissue sections were fixed in 4% PFA and washed with 1x PBS. The tissue was permeabilized with proteinase K at 10μg/mL for 15 min and subsequently washed with 1x PBS. Tissue was then washed in an acetylation solution (0.1 % HCl, 0.375 % Acetic Anhydride, and 0.75 % Triethanolamine in H_20) for 10 min with stirring. Tissue sections were then subsequently washed 3x3min with PBS, rinsed 1x5min in 0.85 % NaCl, 1x5min in 70 % ethanol, and 1x5min in 95 % ethanol prior to riboprobe / hybridization application. Antisense Digoxygenin (DIG) labeled riboprobes were hybridized to the tissue in a solution containing 50% deionized formamide, 2 sodium citrate pH 4.5, 1% SDS, 50μg/mL heparin, 50μg/mL yeast tRNA overnight in a humidity chamber at 68°C. The following day, specimens were treated with successive washes of sodium citrate buffer as described previously,[66] and blocked in 10% heat inactivated sheep serum (HISS), with 2% Roche blocking reagent (BR) in malic acid buffered solution with 0.1% tween-20 (MABT). Anti-DIG-Alkaline Phosphatase (AP) antibody was applied in 1% HISS, 2% BR in MABT overnight at 4°C. The following day the slides were washed in MABT and 100mM NaCl, 100 mM Tris-HCl pH 9.5, 50mM $MgCl_2$, and 0.1 % Tween-20 (NTMT) with 2mM Levamisole to inhibit endogenous alkaline phosphatase activity. Digoxigenin-UTP (Roche 53119620) labeled riboprobes were amplified from cDNA libraries collected from mouse kidney tissue with the following primers:
Podocin forward primer: TGACGTTCCCTTTTTCCATC, Podocin reverse primer with T7 underlined: CAGTGAATTGTAATACGACTCACTATAGGGCTGTGGACAGCGACTGAAGA.
Ildr2 forward: GGAGAATCCTTGGGC and Ildr2 reverse: CAGTGAATTGTAATACGACTCACTATAGGGGTACCCGGCCTTGGC were previously published[66]. Fnbp1l forward primer: GCTGAATGACAATTGTGTGAAC and Fnbp1l reverse: CAGTGAATTGTAATACGACTCACTATAGGGCTGTGCAAGTCCAAGTGTCTTC.

Human kidney tissue

Human kidney tissue samples were de-identified (young) or directly donated (91-year-old) and did not necessitate IRB approval. Young, normal kidney tissue was obtained from the UNC Tissue Procurement Facility as a frozen block. A small piece of tissue was removed with a razorblade, fixed for 10 minutes in 4% paraformaldehyde and subsequent processing for cryosectioning and immunofluorescence carried out as for the mouse (described above). For the old kidney tissue, a fresh sample was excised from the kidney cortex and fixed for 10 minutes in 4% paraformaldehyde prior to processing similar to the young tissue for immunofluorescence.

Abbreviations

4.1 protein, Ezrin, Radixin and Moesin (FERM), Corrected Total Glomerular Florecence (CTGF), E and F helix–Hand (EF-Hand), End Stage Renal Disease (ESRD), Kidney Interactive Transcriptomics (KIT), Gene Ontogeny (GO), Glomerular Basement Membrane (GBM), Mass Spectrometry (MS), PSD-95, Disc large, and ZO – 1 (PDZ), Src homology (SH),

Acknowledgements

We would like to acknowledge the many people and core services at the University of North Carolina at Chapel Hill who aided in this investigation. We specifically would like to thank Wendy Salmon, Director of the Department of Cell Biology and Physiology's Hooker Imaging Core, Laura Herring, Ph.D., Director of the School of Medicine's Michael Hooker Proteomics Center, and Victoria Madden and Kristen White, providers of electron microscopy services in the Department of

740 Pathology and Laboratory Medicine's Microscopy Services Laboratory. Paul Risteff for training in
741 TEM and aid with image acquisition and sample preparation.
742 This research is based in part on work conducted at the Microscopy Services Laboratory
743 (TEM), the UNC Proteomics Core Facility (MS), and the UNC Hooker Imaging Core Facility
744 (confocal microscopy), which are supported in part by P30 CA016086 Cancer Center Core Support
745 Grant to the UNC Lineberger Comprehensive Cancer Center. We would further like to
746 acknowledge the members of the O'Brien lab for critical feedback on these studies. This research
747 was supported in part by a Vanderbilt O'Brien Kidney Center Pilot and Feasibility Award (P30-
748 DK114809), a UNC Junior Faculty Development Award, and Start-Up funds from UNC to LLO as
749 well as F32AR073649 to GFG.
750

751 **References**

752 (1) Quaggin, S. E.; Kreidberg, J. A. Development of the Renal Glomerulus: Good Neighbors and Good
753 Fences. *Development* **2008**, *135* (4), 609–620. https://doi.org/10.1242/dev.001081.
754 (2) Ichimura, K.; Miyazaki, N.; Sadayama, S.; Murata, K.; Koike, M.; Nakamura, K.; Ohta, K.; Sakai, T.
755 Three-Dimensional Architecture of Podocytes Revealed by Block-Face Scanning Electron Microscopy.
756 *Sci Rep* **2015**, *5* (1), 8993. https://doi.org/10.1038/srep08993.
757 (3) Reeves, W.; Caulfield, J. P.; Farquhar, M. G. Differentiation of Epithelial Foot Processes and Filtration
758 Slits: Sequential Appearance of Occluding Junctions, Epithelial Polyanion, and Slit Membranes in
759 Developing Glomeruli. *Lab Invest* **1978**, *39* (2), 90–100.
760 (4) Fukasawa, H.; Bornheimer, S.; Kudlicka, K.; Farquhar, M. G. Slit Diaphragms Contain Tight Junction
761 Proteins. *J Am Soc Nephrol* **2009**, *20* (7), 1491–1503. https://doi.org/10.1681/ASN.2008101117.
762 (5) Reiser, J.; Kriz, W.; Kretzler, M.; Mundel, P. The Glomerular Slit Diaphragm Is a Modified Adherens
763 Junction. *J Am Soc Nephrol* **2000**, *11* (1), 1–8. https://doi.org/10.1681/ASN.V1111.
764 (6) Kestilä, M.; Lenkkeri, U.; Männikkö, M.; Lamerdin, J.; McCready, P.; Putaala, H.; Ruotsalainen, V.;
765 Morita, T.; Nissinen, M.; Herva, R.; Kashtan, C. E.; Peltonen, L.; Holmberg, C.; Olsen, A.;
766 Tryggvason, K. Positionally Cloned Gene for a Novel Glomerular Protein--Nephrin--Is Mutated in
767 Congenital Nephrotic Syndrome. *Mol Cell* **1998**, *1* (4), 575–582. https://doi.org/10.1016/s1097-
768 2765(00)80057-x.
769 (7) Boute, N.; Gribouval, O.; Roselli, S.; Benessy, F.; Lee, H.; Fuchshuber, A.; Dahan, K.; Gubler, M. C.;
770 Niaudet, P.; Antignac, C. NPHS2, Encoding the Glomerular Protein Podocin, Is Mutated in Autosomal
771 Recessive Steroid-Resistant Nephrotic Syndrome. *Nat Genet* **2000**, *24* (4), 349–354.
772 https://doi.org/10.1038/74166.
773 (8) Donoviel, D. B.; Freed, D. D.; Vogel, H.; Potter, D. G.; Hawkins, E.; Barrish, J. P.; Mathur, B. N.;
774 Turner, C. A.; Geske, R.; Montgomery, C. A.; Starbuck, M.; Brandt, M.; Gupta, A.; Ramirez-Solis, R.;
775 Zambrowicz, B. P.; Powell, D. R. Proteinuria and Perinatal Lethality in Mice Lacking NEPH1, a Novel
776 Protein with Homology to NEPHRIN. *Mol Cell Biol* **2001**, *21* (14), 4829–4836.
777 https://doi.org/10.1128/MCB.21.14.4829-4836.2001.
778 (9) Rodewald, R.; Karnovsky, M. J. POROUS SUBSTRUCTURE OF THE GLOMERULAR SLIT
779 DIAPHRAGM IN THE RAT AND MOUSE. *Journal of Cell Biology* **1974**, *60* (2), 423–433.
780 https://doi.org/10.1083/jcb.60.2.423.
781 (10) Karnovsky, M.; Ryan, G. Substructure of the Glomerular Slit Diaphragm in Freeze-Fractured Normal
782 Rat Kidney. *Journal of Cell Biology* **1975**, *65* (1), 233–236. https://doi.org/10.1083/jcb.65.1.233.
783 (11) Miyaki, T.; Kawasaki, Y.; Hosoyamada, Y.; Amari, T.; Kinoshita, M.; Matsuda, H.; Kakuta, S.; Sakai,
784 T.; Ichimura, K. Three-Dimensional Imaging of Podocyte Ultrastructure Using FE-SEM and FIB-SEM
785 Tomography. *Cell Tissue Res* **2020**, *379* (2), 245–254. https://doi.org/10.1007/s00441-019-03118-3.
786 (12) Pagtalunan, M. E.; Miller, P. L.; Jumping-Eagle, S.; Nelson, R. G.; Myers, B. D.; Rennke, H. G.;
787 Coplon, N. S.; Sun, L.; Meyer, T. W. Podocyte Loss and Progressive Glomerular Injury in Type II
788 Diabetes. *J Clin Invest* **1997**, *99* (2), 342–348. https://doi.org/10.1172/JCI119163.
789 (13) van den berg, J. G.; van den Bergh Weerman, M. A.; Assmann, K. J. M.; Weening, J. J.; Florquin, S.
790 Podocyte Foot Process Effacement Is Not Correlated with the Level of Proteinuria in Human

Glomerulopathies. *Kidney International* **2004**, *66* (5), 1901–1906. https://doi.org/10.1111/j.1523-1755.2004.00964.x.

(14) D'Agati, V. Pathologic Classification of Focal Segmental Glomerulosclerosis. *Seminars in Nephrology* **2003**, *23* (2), 117–134. https://doi.org/10.1053/snep.2003.50012.

(15) Kopp, J. B.; Anders, H.-J.; Susztak, K.; Podestà, M. A.; Remuzzi, G.; Hildebrandt, F.; Romagnani, P. Podocytopathies. *Nat Rev Dis Primers* **2020**, *6* (1), 68. https://doi.org/10.1038/s41572-020-0196-7.

(16) Bierzynska, A.; Soderquest, K.; Dean, P.; Colby, E.; Rollason, R.; Jones, C.; Inward, C. D.; McCarthy, H. J.; Simpson, M. A.; Lord, G. M.; Williams, M.; Welsh, G. I.; Koziell, A. B.; Saleem, M. A. *MAGI2* Mutations Cause Congenital Nephrotic Syndrome. *JASN* **2017**, *28* (5), 1614–1621. https://doi.org/10.1681/ASN.2016040387.

(17) Gigante, M.; Pontrelli, P.; Montemurno, E.; Roca, L.; Aucella, F.; Penza, R.; Caridi, G.; Ranieri, E.; Ghiggeri, G. M.; Gesualdo, L. CD2AP Mutations Are Associated with Sporadic Nephrotic Syndrome and Focal Segmental Glomerulosclerosis (FSGS). *Nephrology Dialysis Transplantation* **2009**, *24* (6), 1858–1864. https://doi.org/10.1093/ndt/gfn712.

(18) Liu, Y.-X.; Zhang, A.-Q.; Luo, F.-M.; Sheng, Y.; Wang, C.-Y.; Dong, Y.; Fan, L.; Liu, L. Case Report: A Novel Heterozygous Mutation of CD2AP in a Chinese Family With Proteinuria Leads to Focal Segmental Glomerulosclerosis. *Front. Pediatr.* **2021**, *9*, 687455. https://doi.org/10.3389/fped.2021.687455.

(19) Beltcheva, O.; Martin, P.; Lenkkeri, U.; Tryggvason, K. Mutation Spectrum in the Nephrin Gene (NPHS1) in Congenital Nephrotic Syndrome. *Hum Mutat* **2001**, *17* (5), 368–373. https://doi.org/10.1002/humu.1111.

(20) Guaragna, M. S.; Lutaif, A. C. G. B.; Piveta, C. S. C.; Souza, M. L.; de Souza, S. R.; Henriques, T. B.; Maciel-Guerra, A. T.; Belangero, V. M. S.; Guerra-Junior, G.; De Mello, M. P. NPHS2 Mutations Account for Only 15% of Nephrotic Syndrome Cases. *BMC Med Genet* **2015**, *16*, 88. https://doi.org/10.1186/s12881-015-0231-9.

(21) Lu, C.-C.; Wang, G.-H.; Lu, J.; Chen, P.-P.; Zhang, Y.; Hu, Z.-B.; Ma, K.-L. Role of Podocyte Injury in Glomerulosclerosis. In *Renal Fibrosis: Mechanisms and Therapies*; Liu, B.-C., Lan, H.-Y., Lv, L.-L., Eds.; Advances in Experimental Medicine and Biology; Springer: Singapore, 2019; pp 195–232. https://doi.org/10.1007/978-981-13-8871-2_10.

(22) Pierchala, B. A.; Muñoz, M. R.; Tsui, C. C. Proteomic Analysis of the Slit Diaphragm Complex: CLIC5 Is a Protein Critical for Podocyte Morphology and Function. *Kidney Int* **2010**, *78* (9), 868–882. https://doi.org/10.1038/ki.2010.212.

(23) Kocylowski, M. K.; Aypek, H.; Bildl, W.; Helmstädter, M.; Trachte, P.; Dumoulin, B.; Wittösch, S.; Kühne, L.; Aukschun, U.; Teetzen, C.; Kretz, O.; Gaal, B.; Kulik, A.; Antignac, C.; Mollet, G.; Köttgen, A.; Göcmen, B.; Schwenk, J.; Schulte, U.; Huber, T. B.; Fakler, B.; Grahammer, F. A Slit-Diaphragm-Associated Protein Network for Dynamic Control of Renal Filtration. *Nature Communications* **2022**, *13* (1), 6446. https://doi.org/10.1038/s41467-022-33748-1.

(24) Roselli, S.; Gribouval, O.; Boute, N.; Sich, M.; Benessy, F.; Attié, T.; Gubler, M.-C.; Antignac, C. Podocin Localizes in the Kidney to the Slit Diaphragm Area. *The American Journal of Pathology* **2002**, *160* (1), 131–139. https://doi.org/10.1016/S0002-9440(10)64357-X.

(25) Huber, T. B.; Kottgen, M.; Schilling, B.; Walz, G.; Benzing, T. Interaction with Podocin Facilitates Nephrin Signaling. *J Biol Chem* **2001**, *276* (45), 41543–41546. https://doi.org/10.1074/jbc.C100452200.

(26) Sellin, L.; Huber, T. B.; Gerke, P.; Quack, I.; Pavenstädt, H.; Walz, G. NEPH1 Defines a Novel Family of Podocin Interacting Proteins. *FASEB J* **2003**, *17* (1), 115–117. https://doi.org/10.1096/fj.02-0242fje.

(27) Schwarz, K.; Simons, M.; Reiser, J.; Saleem, M. A.; Faul, C.; Kriz, W.; Shaw, A. S.; Holzman, L. B.; Mundel, P. Podocin, a Raft-Associated Component of the Glomerular Slit Diaphragm, Interacts with CD2AP and Nephrin. *J. Clin. Invest.* **2001**, *108* (11), 1621–1629. https://doi.org/10.1172/JCI200112849.

(28) Schurek, E.-M.; Völker, L. A.; Tax, J.; Lamkemeyer, T.; Rinschen, M. M.; Ungrue, D.; Kratz, J. E.; Sirianant, L.; Kunzelmann, K.; Chalfie, M.; Schermer, B.; Benzing, T.; Höhne, M. A Disease-Causing Mutation Illuminates the Protein Membrane Topology of the Kidney-Expressed Prohibitin Homology

(PHB) Domain Protein Podocin. *Journal of Biological Chemistry* **2014**, *289* (16), 11262–11271. https://doi.org/10.1074/jbc.M113.521773.

(29) Roux, K. J.; Kim, D. I.; Raida, M.; Burke, B. A Promiscuous Biotin Ligase Fusion Protein Identifies Proximal and Interacting Proteins in Mammalian Cells. *Journal of Cell Biology* **2012**, *196* (6), 801–810. https://doi.org/10.1083/jcb.201112098.

(30) Kim, D. I.; Jensen, S. C.; Noble, K. A.; Kc, B.; Roux, K. H.; Motamedchaboki, K.; Roux, K. J. An Improved Smaller Biotin Ligase for BioID Proximity Labeling. *Mol Biol Cell* **2016**, *27* (8), 1188–1196. https://doi.org/10.1091/mbc.E15-12-0844.

(31) Mick, D. U.; Rodrigues, R. B.; Leib, R. D.; Adams, C. M.; Chien, A. S.; Gygi, S. P.; Nachury, M. V. Proteomics of Primary Cilia by Proximity Labeling. *Developmental Cell* **2015**, *35* (4), 497–512. https://doi.org/10.1016/j.devcel.2015.10.015.

(32) Firat-Karalar, E. N.; Rauniyar, N.; Yates, J. R.; Stearns, T. Proximity Interactions among Centrosome Components Identify Regulators of Centriole Duplication. *Curr Biol* **2014**, *24* (6), 664–670. https://doi.org/10.1016/j.cub.2014.01.067.

(33) Rudolph, F.; Fink, C.; Hüttemeister, J.; Kirchner, M.; Radke, M. H.; Lopez Carballo, J.; Wagner, E.; Kohl, T.; Lehnart, S. E.; Mertins, P.; Gotthardt, M. Deconstructing Sarcomeric Structure–Function Relations in Titin-BioID Knock-in Mice. *Nat Commun* **2020**, *11* (1), 3133. https://doi.org/10.1038/s41467-020-16929-8.

(34) Uezu, A.; Kanak, D. J.; Bradshaw, T. W. A.; Soderblom, E. J.; Catavero, C. M.; Burette, A. C.; Weinberg, R. J.; Soderling, S. H. Identification of an Elaborate Complex Mediating Postsynaptic Inhibition. *Science* **2016**, *353* (6304), 1123–1129. https://doi.org/10.1126/science.aag0821.

(35) Roselli, S.; Heidet, L.; Sich, M.; Henger, A.; Kretzler, M.; Gubler, M.-C.; Antignac, C. Early Glomerular Filtration Defect and Severe Renal Disease in Podocin-Deficient Mice. *Molecular and Cellular Biology* **2004**, *24* (2), 550–560. https://doi.org/10.1128/MCB.24.2.550-560.2004.

(36) Sears, R. M.; May, D. G.; Roux, K. J. BioID as a Tool for Protein-Proximity Labeling in Living Cells. *Methods Mol Biol* **2019**, *2012*, 299–313. https://doi.org/10.1007/978-1-4939-9546-2_15.

(37) Asanuma, K.; Campbell, K. N.; Kim, K.; Faul, C.; Mundel, P. Nuclear Relocation of the Nephrin and CD2AP-Binding Protein Dendrin Promotes Apoptosis of Podocytes. *Proc. Natl. Acad. Sci. U.S.A.* **2007**, *104* (24), 10134–10139. https://doi.org/10.1073/pnas.0700917104.

(38) Ebnet, K.; Suzuki, A.; Ohno, S.; Vestweber, D. Junctional Adhesion Molecules (JAMs): More Molecules with Dual Functions? *Journal of Cell Science* **2004**, *117* (1), 19–29. https://doi.org/10.1242/jcs.00930.

(39) Gerlach, G. F.; Wingert, R. A. Zebrafish Pronephros Tubulogenesis and Epithelial Identity Maintenance Are Reliant on the Polarity Proteins Prkc Iota and Zeta. *Developmental Biology* **2014**, *396* (2), 183–200. https://doi.org/10.1016/j.ydbio.2014.08.038.

(40) Seeger, T. S.; Frank, D.; Rohr, C.; Will, R.; Just, S.; Grund, C.; Lyon, R.; Luedde, M.; Koegl, M.; Sheikh, F.; Rottbauer, W.; Franke, W. W.; Katus, H. A.; Olson, E. N.; Frey, N. Myozap, a Novel Intercalated Disc Protein, Activates Serum Response Factor-Dependent Signaling and Is Required to Maintain Cardiac Function in Vivo. *Circ Res* **2010**, *106* (5), 880–890. https://doi.org/10.1161/CIRCRESAHA.109.213256.

(41) Pieperhoff, S.; Rickelt, S.; Heid, H.; Claycomb, W. C.; Zimbelmann, R.; Kuhn, C.; Winter-Simanowski, S.; Kuhn, C.; Frey, N.; Franke, W. W. The Plaque Protein Myozap Identified as a Novel Major Component of Adhering Junctions in Endothelia of the Blood and the Lymph Vascular Systems. *Journal of Cellular and Molecular Medicine* **2012**, *16* (8), 1709–1719. https://doi.org/10.1111/j.1582-4934.2011.01463.x.

(42) Ho, H.-Y. H.; Rohatgi, R.; Lebensohn, A. M.; Le Ma; Li, J.; Gygi, S. P.; Kirschner, M. W. Toca-1 Mediates Cdc42-Dependent Actin Nucleation by Activating the N-WASP-WIP Complex. *Cell* **2004**, *118* (2), 203–216. https://doi.org/10.1016/j.cell.2004.06.027.

(43) Van Itallie, C. M.; Tietgens, A. J.; Krystofiak, E.; Kachar, B.; Anderson, J. M. A Complex of ZO-1 and the BAR-Domain Protein TOCA-1 Regulates Actin Assembly at the Tight Junction. *MBoC* **2015**, *26* (15), 2769–2787. https://doi.org/10.1091/mbc.E15-04-0232.

(44) Wu, H.; Malone, A. F.; Donnelly, E. L.; Kirita, Y.; Uchimura, K.; Ramakrishnan, S. M.; Gaut, J. P.; Humphreys, B. D. Single-Cell Transcriptomics of a Human Kidney Allograft Biopsy Specimen Defines a Diverse Inflammatory Response. *JASN* **2018**, *29* (8), 2069–2080. https://doi.org/10.1681/ASN.2018020125.

(45) Lu, Y.; Ye, Y.; Bao, W.; Yang, Q.; Wang, J.; Liu, Z.; Shi, S. Genome-Wide Identification of Genes Essential for Podocyte Cytoskeletons Based on Single-Cell RNA Sequencing. *Kidney International* **2017**, *92* (5), 1119–1129. https://doi.org/10.1016/j.kint.2017.04.022.

(46) Higashi, T.; Tokuda, S.; Kitajiri, S.; Masuda, S.; Nakamura, H.; Oda, Y.; Furuse, M. Analysis of the "angulin" Proteins LSR, ILDR1 and ILDR2--Tricellulin Recruitment, Epithelial Barrier Function and Implication in Deafness Pathogenesis. *J Cell Sci* **2013**, *126* (Pt 4), 966–977. https://doi.org/10.1242/jcs.116442.

(47) Rodewald, R.; Karnovsky, M. J. POROUS SUBSTRUCTURE OF THE GLOMERULAR SLIT DIAPHRAGM IN THE RAT AND MOUSE. *Journal of Cell Biology* **1974**, *60* (2), 423–433. https://doi.org/10.1083/jcb.60.2.423.

(48) Karnovsky, M.; Ryan, G. Substructure of the Glomerular Slit Diaphragm in Freeze-Fractured Normal Rat Kidney. *Journal of Cell Biology* **1975**, *65* (1), 233–236. https://doi.org/10.1083/jcb.65.1.233.

(49) Kopp, J. B.; Anders, H.-J.; Susztak, K.; Podestà, M. A.; Remuzzi, G.; Hildebrandt, F.; Romagnani, P. Podocytopathies. *Nat Rev Dis Primers* **2020**, *6* (1), 68. https://doi.org/10.1038/s41572-020-0196-7.

(50) Branon, T. C.; Bosch, J. A.; Sanchez, A. D.; Udeshi, N. D.; Svinkina, T.; Carr, S. A.; Feldman, J. L.; Perrimon, N.; Ting, A. Y. Efficient Proximity Labeling in Living Cells and Organisms with TurboID. *Nat Biotechnol* **2018**, *36* (9), 880–887. https://doi.org/10.1038/nbt.4201.

(51) May, D. G.; Scott, K. L.; Campos, A. R.; Roux, K. J. Comparative Application of BioID and TurboID for Protein-Proximity Biotinylation. *Cells* **2020**, *9* (5), 1070. https://doi.org/10.3390/cells9051070.

(52) Wu, H.; Malone, A. F.; Donnelly, E. L.; Kirita, Y.; Uchimura, K.; Ramakrishnan, S. M.; Gaut, J. P.; Humphreys, B. D. Single-Cell Transcriptomics of a Human Kidney Allograft Biopsy Specimen Defines a Diverse Inflammatory Response. *JASN* **2018**, *29* (8), 2069–2080. https://doi.org/10.1681/ASN.2018020125.

(53) Thisse, B., Thisse, C. (2004) Fast Release Clones: A High Throughput Expression Analysis. ZFIN Direct Data Submission. . (Http://Zfin.Org).

(54) McKee, R.; Gerlach, G. F.; Jou, J.; Cheng, C. N.; Wingert, R. A. Temporal and Spatial Expression of Tight Junction Genes during Zebrafish Pronephros Development. *Gene Expr Patterns* **2014**, *16* (2), 104–113. https://doi.org/10.1016/j.gep.2014.11.001.

(55) Podojil, J. R.; Hecht, I.; Chiang, M.-Y.; Vaknin, I.; Barbiro, I.; Novik, A.; Neria, E.; Rotman, G.; Miller, S. D. ILDR2-Fc Is a Novel Regulator of Immune Homeostasis and Inducer of Antigen-Specific Immune Tolerance. *J Immunol* **2018**, *200* (6), 2013–2024. https://doi.org/10.4049/jimmunol.1700326.

(56) Hecht, I.; Toporik, A.; Podojil, J. R.; Vaknin, I.; Cojocaru, G.; Oren, A.; Aizman, E.; Liang, S. C.; Leung, L.; Dicken, Y.; Novik, A.; Marbach-Bar, N.; Elmesmari, A.; Tange, C.; Gilmour, A.; McIntyre, D.; Kurowska-Stolarska, M.; McNamee, K.; Leitner, J.; Greenwald, S.; Dassa, L.; Levine, Z.; Steinberger, P.; Williams, R. O.; Miller, S. D.; McInnes, I. B.; Neria, E.; Rotman, G. ILDR2 Is a Novel B7-like Protein That Negatively Regulates T Cell Responses. *J Immunol* **2018**, *200* (6), 2025–2037. https://doi.org/10.4049/jimmunol.1700325.

(57) Huetter, J.; Gritzan, U.; Gutcher, I.; Doecke, W.-D.; Luetke-Eversloh, M. V.; Golfier, S.; Roider, H. G.; Frisk, A.-L.; Hunter, J.; Pow, A.; Drake, A.; Levine, Z.; Levy, O.; Azulay, M.; Barbiro, I.; Cojocaru, G.; Vaknin, I.; Kreft, B.; Roese, L. Characterization of BAY 1905254, an Immune Checkpoint Inhibitor Targeting the Immunoglobulin-Like Domain Containing Receptor 2 (ILDR2). *Cancer Immunol Res* **2020**, *8* (7), 895–911. https://doi.org/10.1158/2326-6066.CIR-19-0321.

(58) Wu, H.; Kirita, Y.; Donnelly, E. L.; Humphreys, B. D. Advantages of Single-Nucleus over Single-Cell RNA Sequencing of Adult Kidney: Rare Cell Types and Novel Cell States Revealed in Fibrosis. *JASN* **2019**, *30* (1), 23–32. https://doi.org/10.1681/ASN.2018090912.

(59) Ettou, S.; Jung, Y. L.; Miyoshi, T.; Jain, D.; Hiratsuka, K.; Schumacher, V.; Taglienti, M. E.; Morizane, R.; Park, P. J.; Kreidberg, J. A. Epigenetic Transcriptional Reprogramming by WT1 Mediates a Repair

945 Response during Podocyte Injury. *Sci. Adv.* **2020**, *6* (30), eabb5460.
946 https://doi.org/10.1126/sciadv.abb5460.
947 (60) Go, C. D.; Knight, J. D. R.; Rajasekharan, A.; Rathod, B.; Hesketh, G. G.; Abe, K. T.; Youn, J.-Y.;
948 Samavarchi-Tehrani, P.; Zhang, H.; Zhu, L. Y.; Popiel, E.; Lambert, J.-P.; Coyaud, É.; Cheung, S. W.
949 T.; Rajendran, D.; Wong, C. J.; Antonicka, H.; Pelletier, L.; Palazzo, A. F.; Shoubridge, E. A.; Raught,
950 B.; Gingras, A.-C. A Proximity-Dependent Biotinylation Map of a Human Cell. *Nature* **2021**, *595*
951 (7865), 120–124. https://doi.org/10.1038/s41586-021-03592-2.
952 (61) Yu, H. H.; Zallen, J. A. Abl and Canoe/Afadin Mediate Mechanotransduction at Tricellular Junctions.
953 *Science* **2020**, *370* (6520), eaba5528. https://doi.org/10.1126/science.aba5528.
954 (62) Cox, J.; Mann, M. MaxQuant Enables High Peptide Identification Rates, Individualized p.p.b.-Range
955 Mass Accuracies and Proteome-Wide Protein Quantification. *Nat Biotechnol* **2008**, *26* (12), 1367–1372.
956 https://doi.org/10.1038/nbt.1511.
957 (63) Brademan, D. R.; Miller, I. J.; Kwiecien, N. W.; Pagliarini, D. J.; Westphall, M. S.; Coon, J. J.;
958 Shishkova, E. Argonaut: A Web Platform for Collaborative Multi-Omic Data Visualization and
959 Exploration. *Patterns* **2020**, *1* (7), 100122. https://doi.org/10.1016/j.patter.2020.100122.
960 (64) Reynolds, E. S. THE USE OF LEAD CITRATE AT HIGH PH AS AN ELECTRON-OPAQUE STAIN
961 IN ELECTRON MICROSCOPY. *Journal of Cell Biology* **1963**, *17* (1), 208–212.
962 https://doi.org/10.1083/jcb.17.1.208.
963 (65) Hobot, J. A.; Newman, G. R. Immunomicroscopy: Resin Techniques and on-Section Labelling with
964 Immunocolloidal Gold or Immunoperoxidase--Planning a Protocol. *Scanning Microsc* **1996**, *10* (1),
965 121–143; discussion 143-145.
966 (66) Liu, Y.; Nie, H.; Liu, C.; Zhai, X.; Sang, Q.; Wang, Y.; Shi, D.; Wang, L.; Xu, Z. Angulin Proteins
967 ILDR1 and ILDR2 Regulate Alternative Pre-MRNA Splicing through Binding to Splicing Factors
968 TRA2A, TRA2B, or SRSF1. *Sci Rep* **2017**, *7* (1), 7466. https://doi.org/10.1038/s41598-017-07530-z.
969

Figure 1

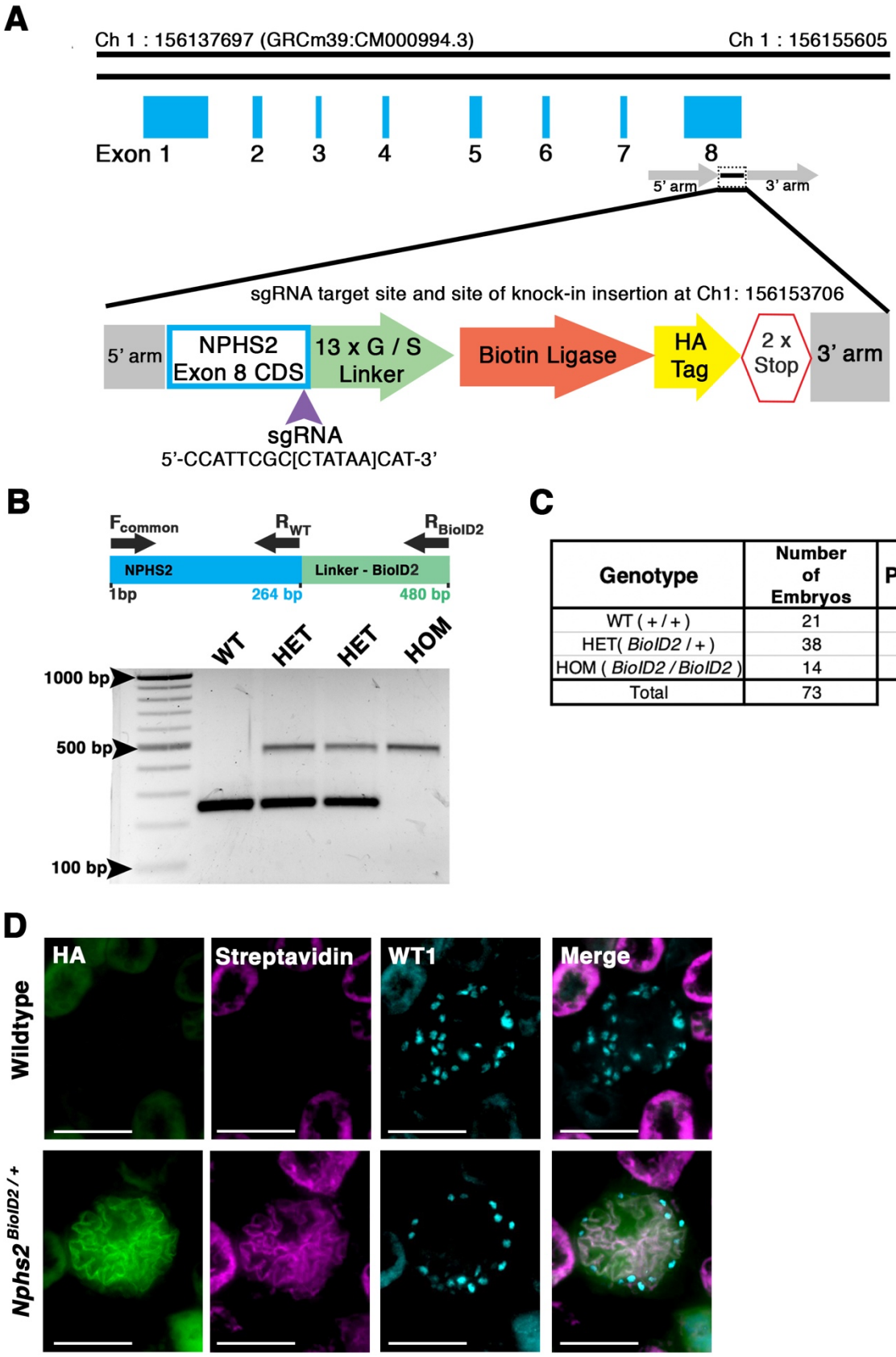

Genotype	Number of Embryos	Percentage
WT (+ / +)	21	29
HET(*BioID2* / +)	38	52
HOM (*BioID2* / *BioID2*)	14	19
Total	73	

970
971

Figure 1. Generation of a knock-in *Nphs2*^{BioID2} mouse line via CRISPR/Cas9 genome editing of the *Nphs2* locus. (A) Schematic of the CRISPR/Cas9 genome editing strategy utilized to generate the *Nphs2*^{BioID2} mouse line. A small guide RNA (sgRNA) targeting the stop codon in exon 8 of *Nphs2* (purple arrowhead) was combined with a donor vector containing the knock-in cassette (zoom view) to induce homologous recombination and integrate the BioID2 moiety containing a 13x Glycine/Serine (G/S) linker, biotin ligase, and HA tag into the *Nphs2* locus. **(B)** Genotyping strategy (top panel) to identify genotype of mice as wildtype (single band at 264 base pairs (bp)), heterozygous (two bands; one at wildtype size of 264 bp and a second that amplifies the BioID2 linker region giving a band at 480 bp), or homozygous (single band at the 480 bp). **(C)** Genotyping of 73 embryos at E18.5-P0, verify an approximate Mendelian ratio of genotypes being recovered (25:50:25). **(D)** IF analysis of 8–10-week-old adult mice injected with biotin illustrate an enrichment of streptavidin detected within the glomerulus of Nphs2^{BioID2} mice and absence of streptavidin signal in control age matched C57BL/6J littermate mice. The HA signal from the BioID2 moiety closely overlaps with streptavidin, observed as white overlap in the merged image. Wilms Tumor (WT1) is utilized as a podocyte marker to delineate the glomerular boundaries. Scale bar: 50 μm

Figure 2.

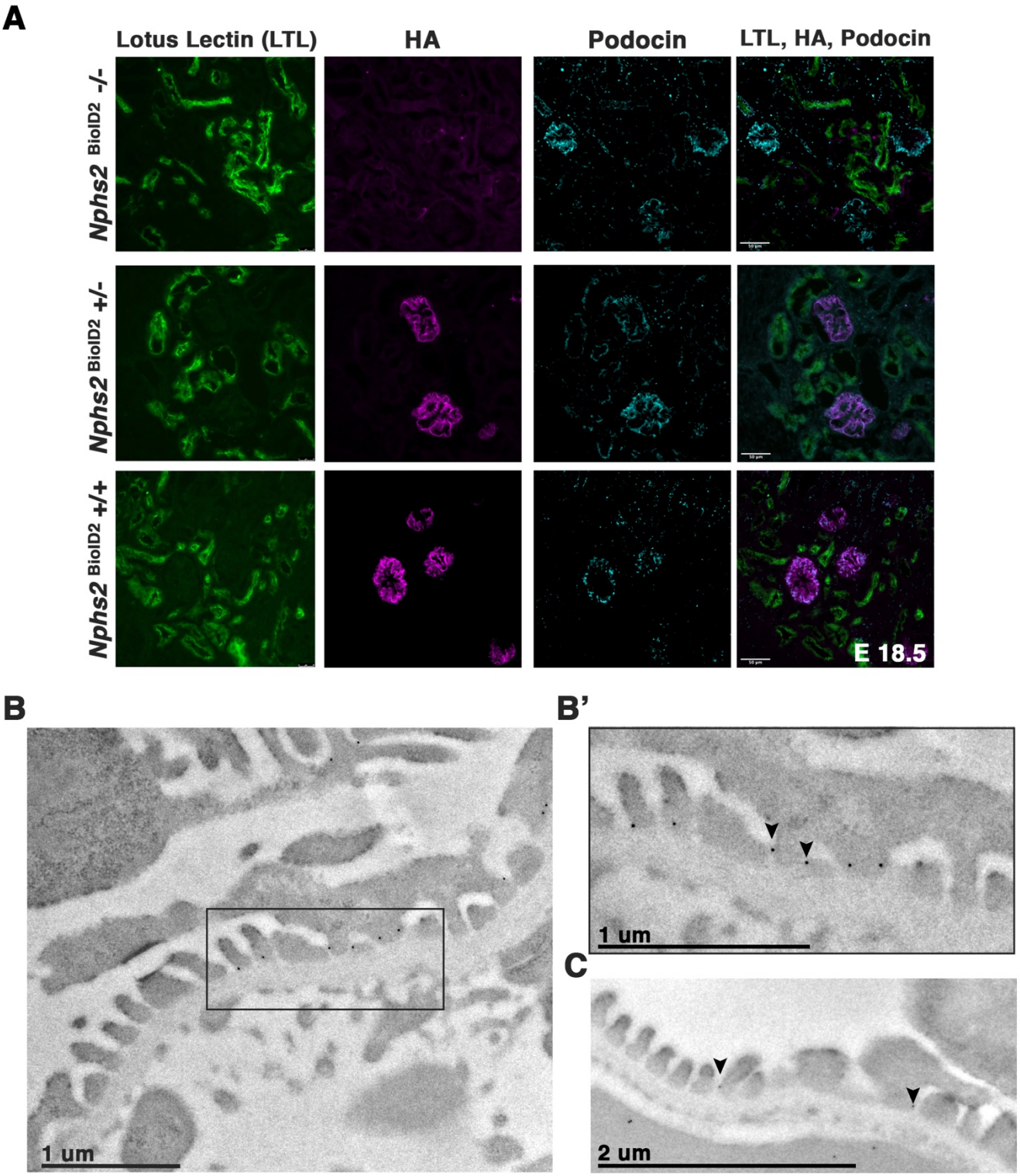
A
Lotus Lectin (LTL)
HA
Podocin
LTL, HA, Podocin
Nphs2 BioID2 -/-
Nphs2 BioID2 +/-
Nphs2 BioID2 +/+
E 18.5
B
B'
C
1 um
1 um
2 um

989

990 **Figure 2. *Nphs2*^{BioID2} animals present normal kidney morphology with podocin-BioID**
991 **localized to podocytes and specifically the slit diaphragm. (A)** E18.5 littermates of wildtype,
992 heterozygous (*Nphs2*$^{BioID2/+}$), and homozygous (*Nphs2*$^{BioID2/BioID2}$) animals were analyzed for gross
993 kidney morphology and localization of podocin-BioID. The proximal tubule marker lotus lectin (LTL,
994 green) show normal tubule architecture without observation of nephron tubule dilation in
995 heterozygous (*Nphs2*$^{BioID\ /+}$), and homozygous (*Nphs2*$^{BioID2\ /\ BioID2}$) animals. The HA tag (magenta)
996 which is part of the BioID2 moiety was observed to tightly overlap with podocin (cyan) specifically
997 in the glomerulus. The relative size and number of glomeruli was unchanged between control,
998 heterozygous, and homozygous animals. Further, the HA signal was not identified outside of the
999 glomeruli. Scale bar 50 μm **(B)** *Nphs2*$^{BioID2/+}$ localizes to the podocyte slit diaphragm. Utilizing
1000 transmission electron microscopy (TEM) and immunogold labeling of 4-week-old murine kidney
1001 samples, we detect the anti-HA signal as punctate dots strung just above the GBM adjacent to the
1002 podocyte foot process within electron dense regions where the slit diaphragm bridges neighboring
1003 foot processes. **(B')** Magnified view of boxed region from panel (B) depicting podocyte foot
1004 processes and the electron dense regions between them where the HA signal localizes as dark
1005 spherical dots from immunogold labeling, denoted with arrowheads. Scale bar 1 μm **(C)** Wildtype
1006 littermates were immunogold labeled for podocin and similarly display localization of podocin at
1007 electron dense regions between podocyte foot processes, highlighted with arrowheads. Scale bar
1008 2 μm.
1009
1010
1011
1012
1013
1014
1015
1016
1017
1018
1019
1020
1021
1022
1023
1024
1025
1026
1027
1028
1029
1030
1031
1032
1033
1034
1035
1036
1037
1038
1039

Figure 3

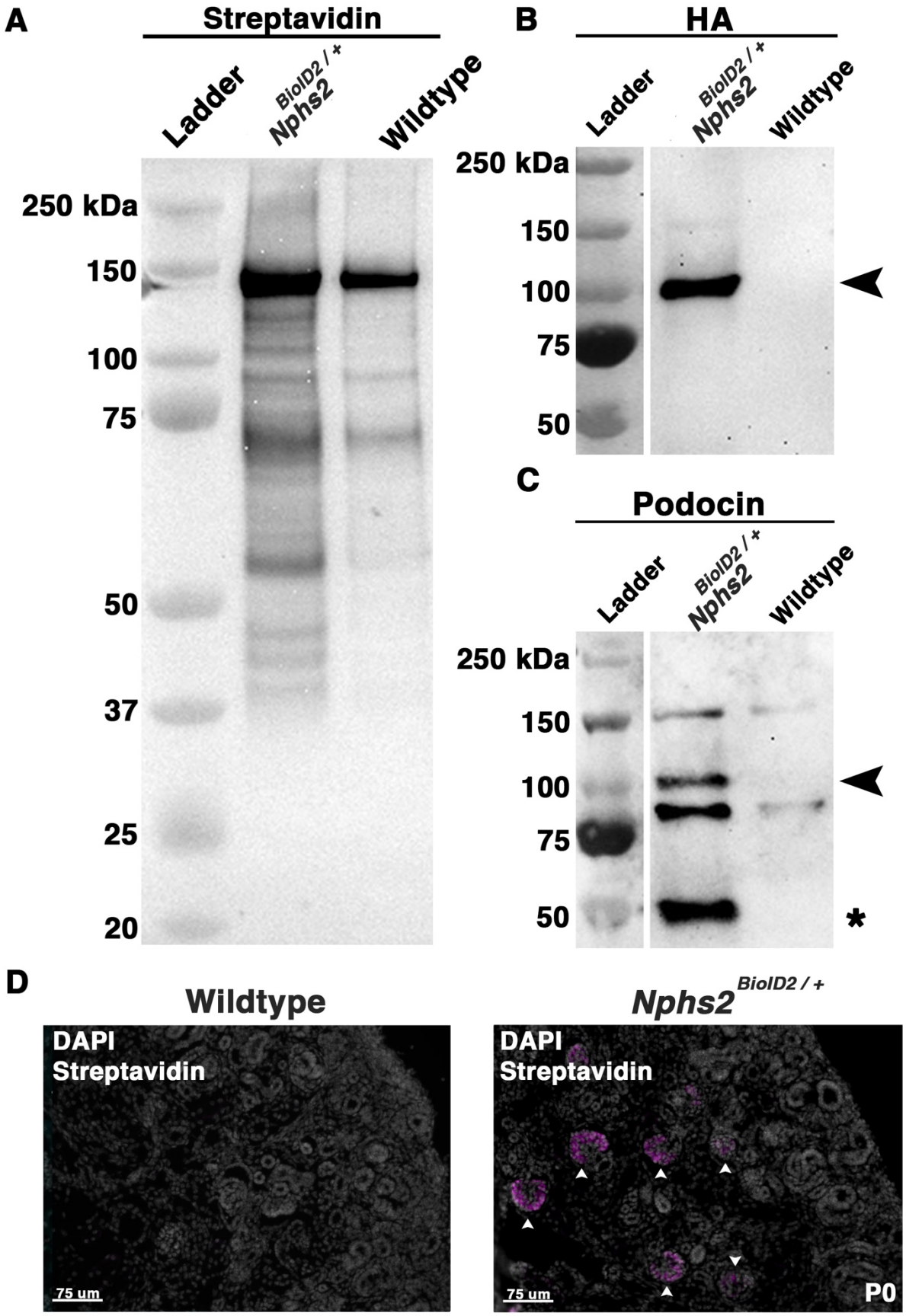

040
041

042 **Figure 3. Biotin administered *Nphs2*$^{BioID2/+}$ mice present an enrichment of biotinylated**
043 **proteins specifically within glomeruli. (A)** A significant enrichment of streptavidin labeled,
044 biotinylated, proteins are observed across the entire molecular weight spectrum in *Nphs2*$^{BioID2/+}$
045 protein lysates compared to wildtype control littermates, injected with biotin. Streptavidin bead
046 purified lysates were subjected to protein separation and probed for streptavidin. Wildtype age
047 matched, 8–10-week-old, littermate controls present few streptavidin conjugated bands,
048 presumably endogenous metabolic carboxylases. However, *Nphs2*$^{BioID2/+}$ lysates exhibit numerous
049 specific biotinylated protein bands across the entire molecular weight spectrum. **(B)** *Nphs2*$^{BioID/+}$
050 lysates blotted with an anti-HA antibody present robust and specific detection of the HA signal only
051 within the *Nphs2*$^{BioID2/+}$ sample, indicative of lysate purity. The HA signal is evident at approximately
052 100 kDa (arrowhead) in *Nphs2*$^{BioID2/+}$ lysates. **(C)** *Nphs2*$^{BioID2/+}$ samples probed for podocin show
053 two specific bands for both BioID2-tagged podocin and endogenous podocin. Adult 8-10-week-old
054 *Nphs2*$^{BioID2/+}$ mice blotted for podocin present a 50kDa band for the endogenous unmodified
055 podocin protein, marked with an asterisk (*) and a second larger band at approximately 100 kDa
056 for the HA tagged podocin-BioID of *Nphs2*$^{BioID2/+}$ mice (arrowhead). **(D)** P0 pups collected from
057 pregnant dams injected with 5 mg/kg of biotin every day from E11.5 to E18.5, and without injection
058 of newborn pups, manifest strong streptavidin detection within glomeruli. Immunofluorescence
059 analysis reveals an enrichment of streptavidin signal (magenta) specifically within the glomeruli
060 (arrowheads) of *Nphs2*$^{BioID2/+}$ kidneys compared to wildtype. Scale bar 75 μm.

061
062
063
064
065
066
067
068
069
070
071
072
073
074

Figure 4.

A

Gene Symbol	Protein Names	*p*-Value	Log_2 Fold Change
Kirrel	Kin of IRRE-like protein 1	0.0006	7.75
Tjp1	Tight junction protein ZO-1	0.002	7.63
Nphs2	Podocin	0.019	6.70
Pard3b	Partitioning defective 3 homolog B	0.008	6.39
Magi2	Membrane-associated guanylate kinase, WW and PDZ domain-containing protein 2	0.018	6.29
Cttn	Src substrate cortactin	0.001	5.60
Ddn	Dendrin	0.003	5.56
Nebl	LIM zinc-binding domain-containing Nebulette	0.010	4.93
Ildr2	Immunoglobulin-like domain-containing receptor 2	0.007	4.90
Fnbp1l	Formin-binding protein 1-like	0.014	4.27
Synpo	Synaptopodin	0.047	2.90
Tjp2	Tight junction protein ZO-2	0.014	4.71
Myzap	Myocardial zonula adherens protein	0.009	3.45
Cd2ap	CD2-associated protein	0.020	3.18
Col1a1	Collagen alpha-1(I) chain	0.007	2.05
Aif1l	Allograft inflammatory factor 1-like	0.014	1.86
Tns2	Tensin-2	0.022	1.75

B

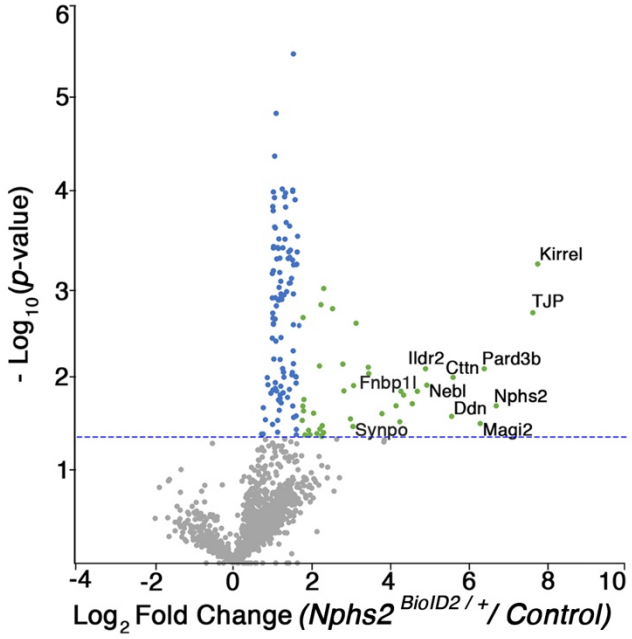

C

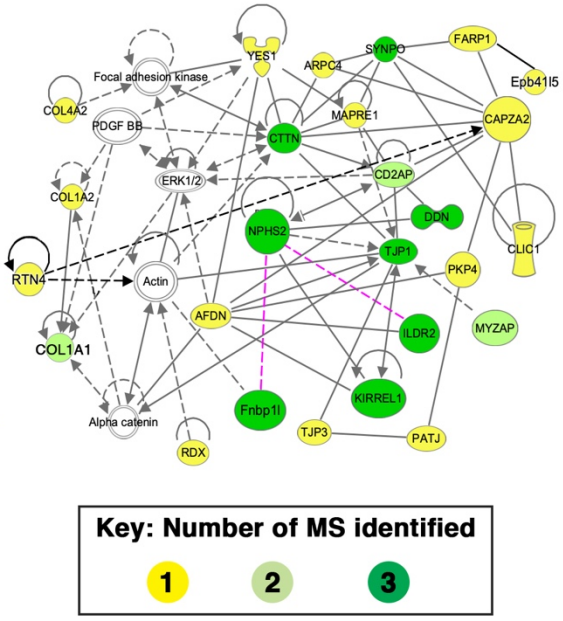

D

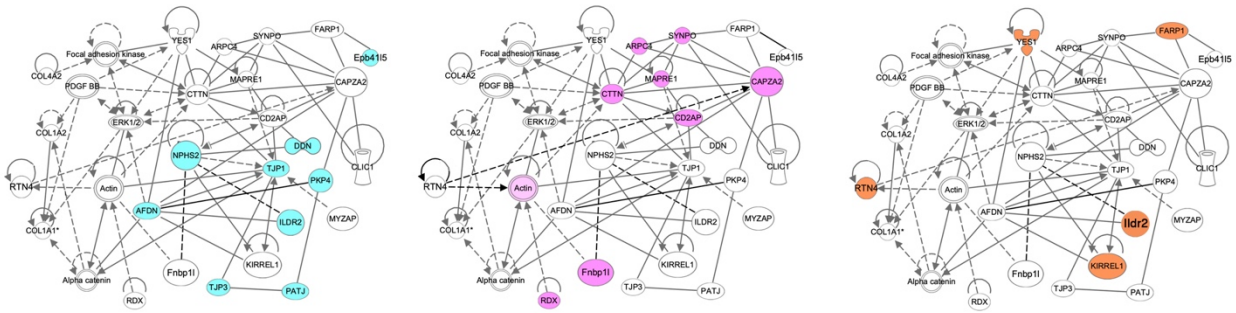

075
076

Figure 4. Proteomics profiling of the podocyte foot process identifies documented slit diaphragm components and novel candidates with unexplored podocyte function. (A) Three separate MS analyses were combined, and the average Log_2 fold change and respective *p*-values were averaged to produce a list of the top foot process proteins. The top 11 proteins were identified across all three MS profiles. Six additional proteins were identified across two of the three MS analyses, denoted following the thick black bar. Podocin was a top protein identified and known to oligomerize, indicating our MS proteomic profiling was effective. Additionally, many of the top proteins uncovered, *i.e.*, Kirrel, Dnd, Tjp1/2, Magi2, Pard3, Synpo, and Cd2ap are documented podocyte slit diaphragm components. **(B)** A volcano plot depicting approximately 1400 proteins identified across all three MS analyses. Green dots represent the 40 proteins identified across three separate MS profiles as having a Log_2 fold change ≥ 1.7, and *p*-value ≤ 0.05, blue dots denote all proteins identified to have a significant *p*-value ≤ 0.05, and grey dots are proteins with a *p*-value ≥ 0.05. The top 11 proteins consistently uncovered across all MS analyses are embedded with gene symbols in the plot. The blue dotted line represents a *p*-value ≤ 0.05. **(C)** Network topology was generated utilizing *Qiagen Ingenuity Pathway Analysis* (IPA) on the top 54 proteins from our cumulative proteomic profiles. IPA produces a proposed web of relationships from published literature with most of our top proteins represented, (11 of 17), with documented connections to other foot process and slit diaphragm components. The color intensities of each protein (yellow to green) represent the number of MS analyses from which each protein was identified. Darkest green shade=all three MS analyses, lighter green shade=two of three MS analyses, and yellow=a single MS analysis. Dotted lines and unshaded proteins represent predicted interactions / interactors from IPA analysis, respectively. Magenta lines are novel proteins identified in this study to be present within the podocyte foot process. **(D)** Dissecting the IPA network, identifies three central nodes representing junctions, cytoskeleton, and signaling. Each respective node is color coded with junctions in cyan, cytoskeleton in magenta, and signaling in orange. These computational network topologies and nodes tightly align with podocyte structure and function.

Figure 5.

A

Gene Ontology (GO) Category	Cluster	Enrichment Score	Counts	*p*-Value
Molecular Function (MF)	Cytoskeletal Protein Binding	4.53	12	2.20×10^{-7}
	Actin Binding		6	7.80×10^{-5}
Cellular Component (CC)	Cell-Cell Junction	4.42	12	7.70×10^{-8}
	Adherens Junction		10	7.90×10^{-6}
Biological Process (BP)	Cytoskeleton Organization	2.61	14	3.20×10^{-7}
	Actin Filament-Based Process		12	8.70×10^{-8}

B

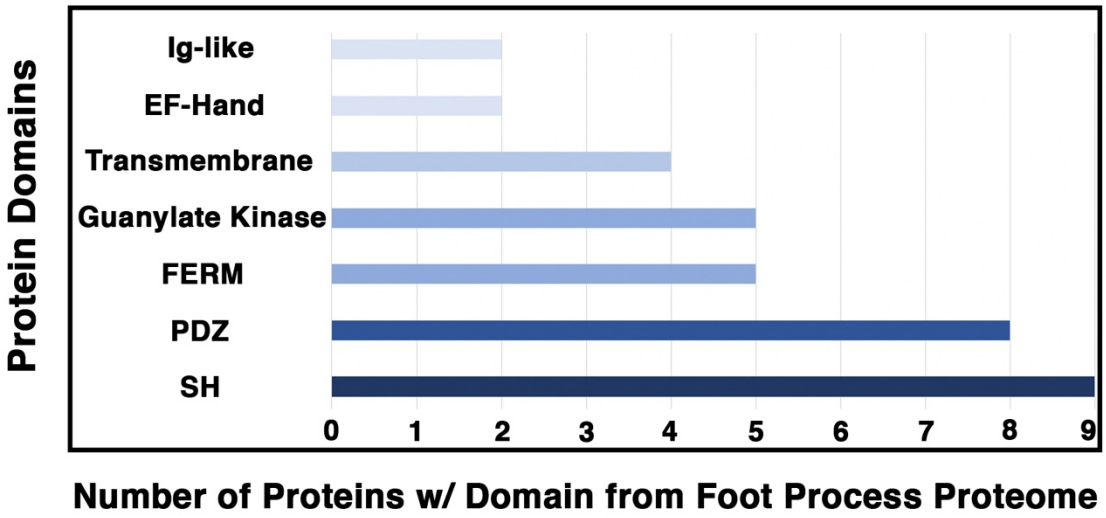

Figure 5. Analysis of the podocyte foot process proteome identifies the cytoskeleton, cell-cell junctions, and actin-based processes as the top GO categories with respective protein domains that align with these functions. The Database for Annotation, Visualization, and Integrative Discovery (DAVID) was utilized for GO clustering analysis of the top 54 proteins identified to have a Log_2 fold change $\geq$ 1.20, and *p*-value $\leq$ 0.05 (Supplemental Table V). **(A)** Overlap in GO readout was observed across the three separate GO categories analyzed, molecular function, cellular component, and biological process, with cytoskeleton, actin, and cellular junctions being the top hits. The respective top clusters within each GO category are listed, alongside the relative enrichment score, number of proteins, and *p*-values. **(B)** Protein domain analysis of the top 54 podocyte foot process proteins provides evidence for protein-protein interactions and likely scaffold and protein-protein complex formation. Each protein's respective protein domains were binary counted for presence or absence within the proteomics profile. The top seven protein domains identified from the podocyte foot process proteome consist of a Src homology (SH) (n = 9 proteins), PSD-95, Disc large, and ZO – 1 (PDZ) (n = 8), 4.1 protein, Ezrin, Radixin and Moesin (FERM) (n = 5), Guanylate Kinase (n = 5), Transmembrane (n = 4), E and F helix – Hand (EF – Hand) (n = 2), and an Immunoglobulin - like (Ig – like) domain (n = 2). Cumulatively, these 7 domains represent ~ 50 % of the top proteins identified from the foot process proteome (26 / 54).

Figure 6.

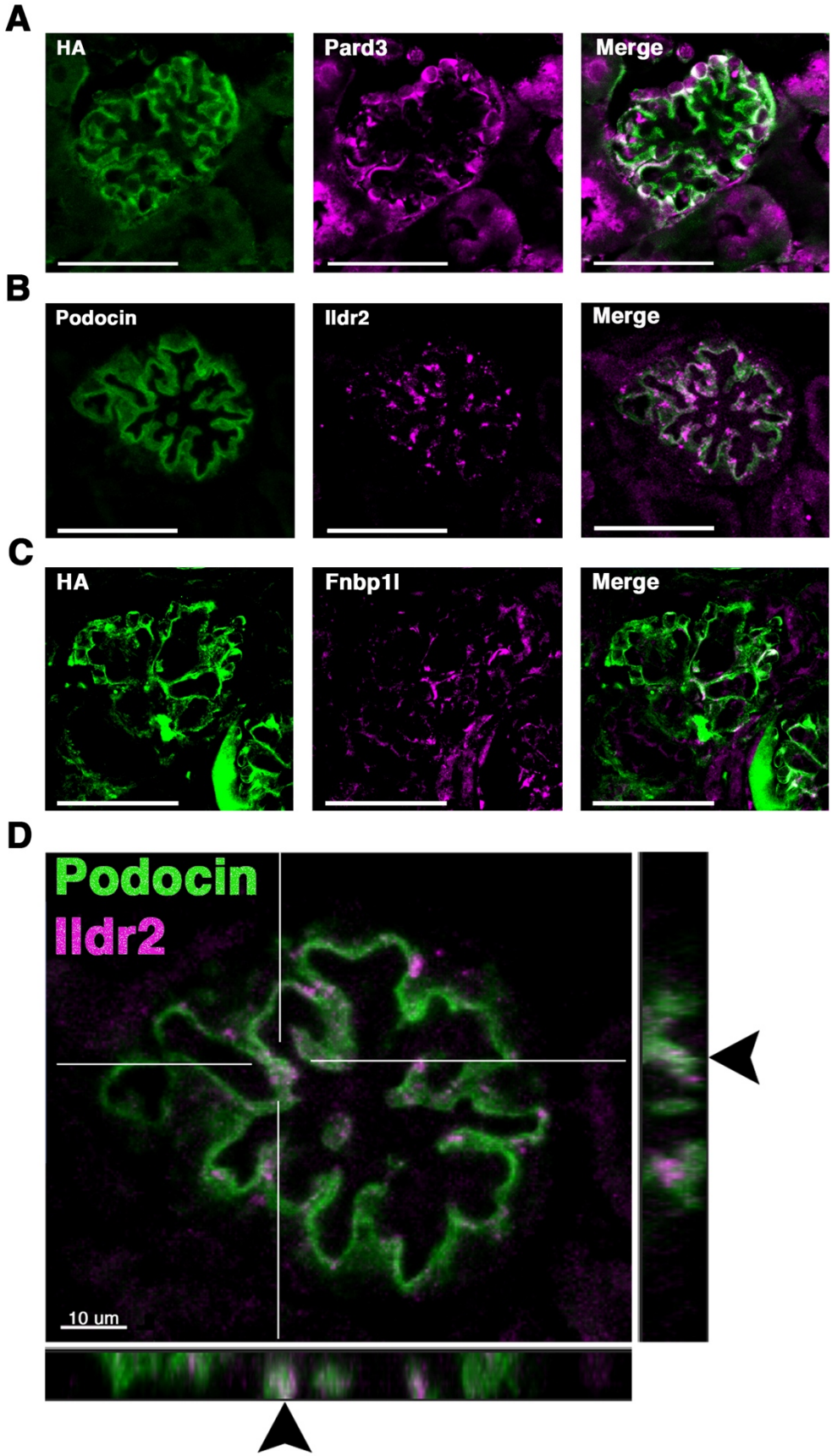
A
HA
Pard3
Merge
B
Podocin
Ildr2
Merge
C
HA
Fnbp1l
Merge
D
Podocin
Ildr2
10 um

Figure 6. Two novel foot process candidates, Ildr2 and Fnbp1l, localize to podocytes and overlap with podocin in the foot process. IF analysis of three top candidates identified from the proteomics profiling, Pard3, Ildr2, and Fnbp1l, were detected within glomeruli. **(A)** Pard3 (magenta), a known component of the podocyte foot process, co-localizes with HA signal of podocin-BioID (green) producing a white signal in overlap. **(B)** Ildr2 (magenta) displays a punctate localization pattern within the glomerulus and overlaps (white) with podocin (green). **(C)** Fnbp1l (magenta) co-localizes (white) with HA signal of podocin-BioID (green) in podocytes. Scale bars in A-C: 50 μm **(D)** A merged image of podocin and Ildr2 through a confocal z-projection identifies punctate localization and overlap (white, arrowheads) between podocin (green) and Ildr2 (magenta) visualized in the z-plane in the left and bottom panels. Scale bar in D 10 μm.

Figure 7.

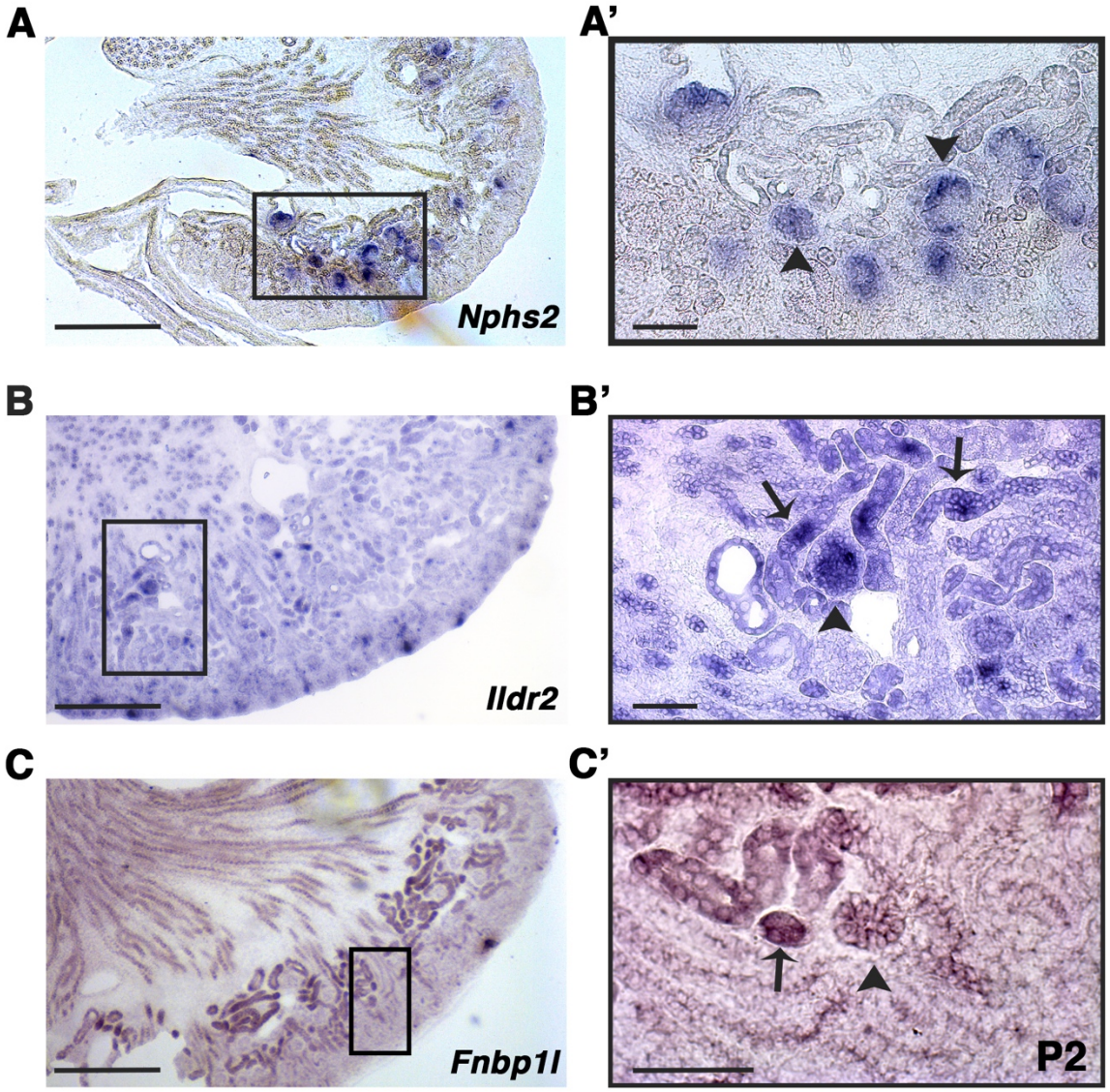

Figure 7. *In situ* hybridization confirms glomerular and some tubule cell expression of *Ildr2* and *Fnbp1l* in P2 kidneys. P2 kidney sections were hybridized with antisense riboprobes against *Nphs2* (podocin)**,** *Ildr2***,** and *Fnbp1l*. **(A)** *Nphs2* (purple) displays strong expression specifically in glomeruli at P2. The rectangular box in **(A)** is enlarged in **(A')** to highlight expression of *Nphs2* only in glomeruli, arrowheads denote example glomeruli **(B)** *Ildr2* transcripts (purple) are identified within glomeruli and tubules. The rectangular box in **(B)** is enlarged in **(B')** to denote expression of *Ildr2* in glomeruli, arrowhead, and in some tubules, black arrow. **(C)** *Fnbp1l* (purple) is identified in both glomeruli and tubules. The block rectangular box in **(C)** is enlarged in **(C')** to denote expression of *Fnbp1l* in glomeruli, arrowhead, and tubules, arrow. Scale bars in A–C: 500 μm. Scale bars in A'-C': 100 μm.

Figure 8.

A

Gene Symbol	Protein Names	BioID (Young) vs WT Log_2 Fold Change	BioID (Aged) vs WT Log_2 Fold Change	*p*-Value
Ildr2	Immunoglobulin-like domain-containing receptor 2	2.76	3.53	0.001
Tjp2	Tight junction protein ZO-2	2.71	3.31	0.01
Pkp4	Plakophilin-4	2.27	2.94	0.01
Nphs2	Podocin	2.42	2.36	0.10
Fnbp1l	Formin-binding protein 1-like	3.22	2.12	0.10
Tns2	Tensin-2	1.30	0.36	0.10

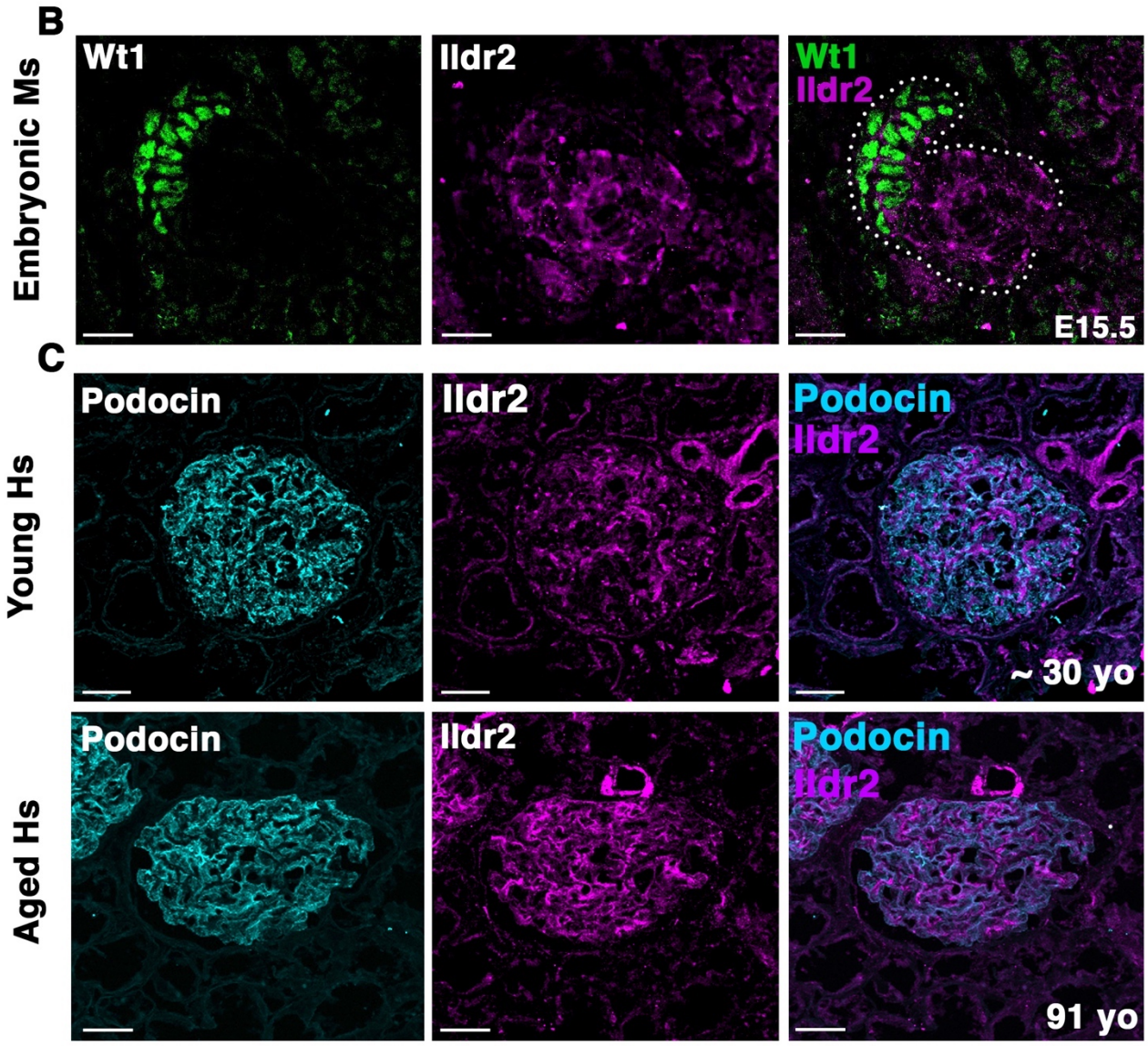

Figure 8. Ildr2 is detected in developing nephron structures and presents increased detection in aged mouse and human glomeruli compared to young. (A) Proteomic profiling of two aged (108 week old) male *Nphs2*$^{BioID2/+}$ mice identifies a significant increase in Ildr2, Tjp2, and Pkp4 protein levels compared to 8-10 week old *Nphs2*$^{BioID2/+}$ mice**.** Table lists 6 proteins with relative detection in "young" 8-10 week old *Nphs2*$^{BioID2/+}$ male mice vs "aged" 108 week old *Nphs2*$^{BioID2/+}$ male mice. All protiens were detected with at least 2 razor unique peptides with their respective *p*-values in far right column. **(B)** Ildr2 is expressed in early developing nephron structures including the renal vesicle, comma, and s-shaped bodies with podocytes denoted by the Wt1-positive nuclei. Ildr2 (magenta) is observed as membranous along the comma / s-shapped body with some punctate foci in E15.5 mouse kidney cortex, outlined with white dots. Scale bar: 20 μm**. (C)** Young and aged (91 yo) human kidney tissue was probed of Ildr2 via IF. Young human glomeruli display punctate foci detection of Ildr2 (magenta) similar to 8-10 week old mice. However, aged (91 yo) male glomeruli evince an increase in Ildr2 detection within glomeruli. Furthermore, where Ildr2 looks to be more highly detected in these aged glomeruli podocin appears less detectable. Scale bar: 50 μm.

Figure 9

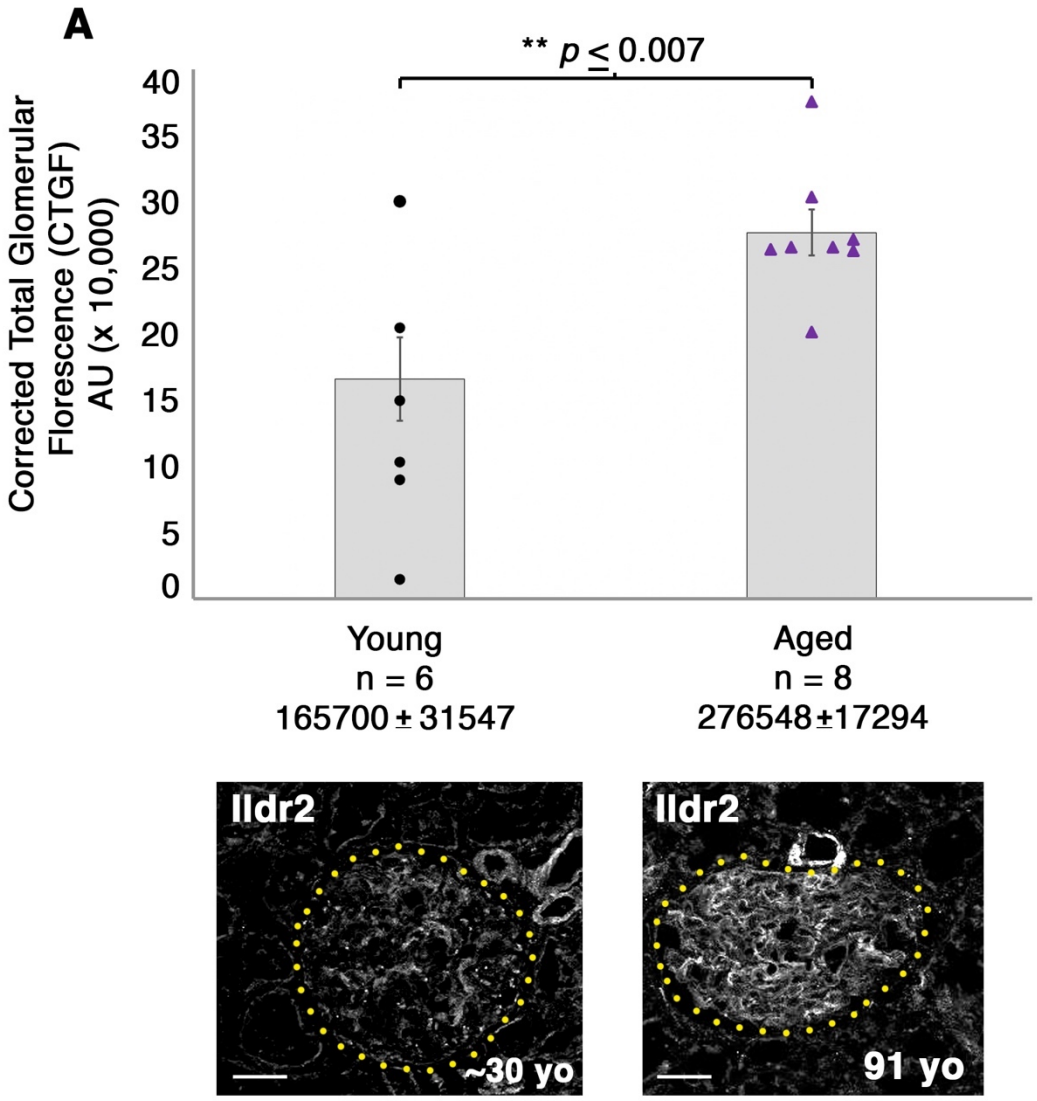
A
** p ≤ 0.007
Corrected Total Glomerular Florescence (CTGF) AU (x 10,000)
40
35
30
25
20
15
10
5
0
Young
n = 6
165700 ± 31547
Aged
n = 8
276548 ±17294
lldr2
~30 yo
lldr2
91 yo

Figure 9. Aged 91 yo glomeruli exhibit a significant increase in corrected total glomerular florecence (CTGF) compared to young human glomeruli. We observe a significant ($p \leq 0.007$) increase, of approximatly 67%, in CTFG in aged human lldr2 detection compared to young human tissue. CTGF was calculated by selecting the gomeruli as the ROI then measuring the total florescence within the area and subtracting out the sum of the area by the average background florecence, *i.e.* Total gROI florecence – (Area of glomerulus *x* mean of background florescence) = CTGF. Two example glomeruli are displayed and outlined in yellow dots to depict the respective ROI utilized to calculate CTGF. Scale bar: 50 μm.

Supplemental Table I.

Antidody	Dilution [IF]	Dilution [WB]	Company
Goat anti - Collagen IV	[1:500]		Sigma-Aldrich, AB769, Lot 2930544
Mouse (IgG1) anti - Myozap	supernatant (straight)		Progen, clone 517.67, 651169
Rabbit anti - F11r (Jam1)	[1:50]		ABclonal, A1241, Lot 0005180101
Rabbit anti - Fnbp1l (Toca-1)	[1:100]		Bethyl Laboratories, A303-469A, Lot 1
Rabbit anti - HA	[1:500]	[1:1000]	Cell Signaling, clone C29F4, 3724S
Rabbit anti - Ildr2	[1:250]		BiCell Scientific Inc, 00303
Rabbit anti - Ildr2	[1:50]		Lifespan BioSciences LS-C205504
Rabbit anti - Ildr2	[1:50]		Invitrogen, PA5-46481, Lot WE327570
Rabbit anti - Pard3	[1:250]		Sigma-Aldrich, 07-330, Lot 2615671
Rabbit anti - podocin	[1:500]	[1:1000]	Invitrogen, PA5-79757, Lot WL3458408
Rabbit anti - WT1	[1:500]		Abcam, ab89901, LotGR3365362-7
Lotus Lectin	[1:1000]		Vector Laboratories, FL-1321, Lot ZC0914
Streptavidin - APC	[1:1000]		BD Pharmingen, 554067 Lot 7040924
Streptavidin - HRP		[1:5000]	Cell Signaling, 3999S, Lot 8

199 **Supplemental Table I. List of antibodies with respective company identifiers and**
200 **concentrations for immunoflorecence (IF) and western blot (WB) analyses utilized in this**
201 **investigation.**

Supplemental Table II.

Gene Symbol	Majority Protein IDs	Protein Names	Razor + Unique Peptides	Log_2 Fold Change	*p* - Value
Nphs2	Q91X05	Podocin	12	10.63	0.00003
Tjp1	P39447	Tight junction protein ZO-1	85	7.40	0.001
Magi2	Q9WVQ1	Membrane-associated guanylate kinase, WW and PDZ domain-containing protein 2	33	7.37	0.001
Kirrel	Q80W68	Kin of IRRE-like protein 1	20	7.06	0.001
Pard3b	Q9CSB4	Partitioning defective 3 homolog B	32	5.34	0.00002
Ddn	Q80TS7	Dendrin	12	5.33	0.00003
Ildr2	B5TVM2	Immunoglobulin-like domain-containing receptor 2	11	4.51	0.009
Cttn	Q60598	Src substrate cortactin	15	4.01	0.0003
Nebl	Q9DC07	LIM zinc-binding domain-containing Nebulette	11	3.65	0.003
Tjp2	Q9Z0U1	Tight junction protein ZO-2	31	3.63	0.021
S100g	P97816	Protein S100-G	4	3.06	0.034
Fnbp1l	Q8K012	Formin-binding protein 1-like	7	2.92	0.010
Capza2	P47754	F-actin-capping protein subunit alpha-2	8	2.82	0.014
Atp6v1e1	P50518	V-type proton ATPase subunit E 1	9	2.30	0.039
Canx	P35564	Calnexin	9	2.26	0.042
Myzap	Q3UIJ9	Myocardial zonula adherens protein	7	2.09	0.0001
Kpnb1	P70168	Importin subunit beta-1	2	1.96	0.041
Dars	Q922B2	Aspartate--tRNA ligase, cytoplasmic	7	1.88	0.029
Cndp2	Q9D1A2	Cytosolic non-specific dipeptidase	6	1.83	0.041
Pls3	Q99K51	Plastin-3	5	1.76	0.029
Sult1d1	Q3UZZ6	Sulfotransferase 1 family member D1	5	1.73	0.038
Uqcr10	Q8R1I1	Cytochrome b-c1 complex subunit 9	3	1.67	0.048
Uba52	P62984; P62983; P0CG49; P0CG50	Ubiquitin-60S ribosomal protein L40	5	1.60	0.041
Sec23a	Q01405	Protein transport protein Sec23A	7	1.59	0.030
Cisd2	Q9CQB5	CDGSH iron-sulfur domain-containing protein 2	2	1.46	0.026
Naca	Q60817;P70670	Nascent polypeptide-associated complex subunit alpha, muscle-specific form	2	1.46	0.049
Ca15	Q99N23	Carbonic anhydrase 15	3	1.44	0.050
Qars	Q8BML9	Glutaminyl-TRNA Synthetase 1	2	1.40	0.039
Rpl35	Q6ZWV7	60S ribosomal protein L35	4	1.37	0.038
Agk	Q9ESW4	Acylglycerol kinase, mitochondrial	5	1.37	0.039
Scp2	P32020	Non-specific lipid-transfer protein	13	1.36	0.026
Aimp1	P31230	Endothelial monocyte-activating polypeptide 2	2	1.26	0.046
Dhrs7b	Q99J47	Dehydrogenase/reductase SDR family member 7B	5	1.24	0.024
Fabp4	P04117	Fatty acid-binding protein, adipocyte	2	1.17	0.012
Mpv17	P19258	Protein Mpv17	2	1.15	0.007
Sf3b1	Q99NB9	Splicing factor 3B subunit 1	4	1.10	0.039
Dkc1	Q9ESX5	H/ACA ribonucleoprotein complex subunit 4	4	1.06	0.003
Por	P37040	NADPH--cytochrome P450 reductase	11	1.05	0.031
Synpo	Q8CC35	Synaptopodin	6	1.02	0.054
Acox1	Q9R0H0	Peroxisomal acyl-coenzyme A oxidase 1	24	1.01	0.015
Cisd1	Q91WS0	CDGSH iron-sulfur domain-containing protein 1	6	0.99	0.036

Supplemental Table II. Proteomic profiling of cohort 1, 8-10 week old *Nphs2*^{BioID2} male mice, identifies 41 significantly detected podocyte foot process proteins. MS analysis of biotin administered male *Nphs2*$^{BioID2/+}$ mice identifies Podocin, Tjp, Magi, Kierrel, and Pard3 as top 5 proteins respectively. Table list 41 significant proteins ($p \leq 0.05$) at a Log_2 cut off 1.0 with their respective *p*-values in the far-right column. Podocin was identified as the top hit and is documented to oligomerize with itself adding confidence that the MS analysis was successful. All proteins were identified with at least 2 razor unique peptide sequences *i.e.*, two peptide sequences aligned only to that protein.

Supplemental Table III.

Gene Symbol	Majority Protein IDs	Protein Names	Razor + Unique Peptides	Log_2 Fold Change	*p* - Value
Kirrel	Q80W68	Kin of IRRE-like protein 1+D3:D62	15	10.19	0.001
Tjp1	P39447	Tight junction protein ZO-1	85	9.88	0.003
Pard3b	Q9CSB4	Partitioning defective 3 homolog B	26	9.62	0.016
Ddn	Q80TS7	Dendrin	11	8.99	0.005
Magi2	Q9WVQ1	Membrane-associated guanylate kinase, WW and PDZ domain-containing protein 2	24	8.61	0.011
Nebl	Q9DC07	LIM zinc-binding domain-containing Nebulette	7	7.75	0.021
Iidr2	B5TVM2	Immunoglobulin-like domain-containing receptor 2	9	7.42	0.010
Cttn	Q60598	Src substrate cortactin	14	7.08	0.020
Nphs2	Q91X05	Podocin	10	7.05	0.023
Fnbp1l	Q8K012	Formin-binding protein 1-like	5	6.65	0.008
Magi1	Q6RHR9	Membrane-associated guanylate kinase, WW and PDZ domain-containing protein 1	6	5.89	0.002
Tjp2	Q9Z0U1	Tight junction protein ZO-2	30	5.78	0.006
Myzap	Q3UIJ9	Myocardial zonula adherens protein	4	4.80	0.018
Synpo	Q8CC35	Synaptopodin	4	4.79	0.043
Khsrp	Q3U0V1	Far upstream element-binding protein 2	5	4.69	0.014
Mapre1	Q61166	Microtubule-associated protein RP/EB family member 1	4	4.56	0.019
Yes1	Q04736	Tyrosine-protein kinase Yes	8	4.34	0.015
Tmem65	Q4VAE3	Transmembrane protein 65	4	4.25	0.030
Cd2ap	Q9JLQ0	CD2-associated protein	5	4.15	0.019
Ap1g1	P22892	AP-1 complex subunit gamma-1	6	3.85	0.018
Ewsr1	Q61545	RNA-binding protein EWS	2	3.83	0.038
Oxsm	Q9D404	3-oxoacyl-[acyl-carrier-protein] synthase, mitochondrial	4	3.77	0.033
Erlin2	Q8BFZ9	Erlin-2	6	3.44	0.008
Epb41l5	Q8BGS1	Band 4.1-like protein 5	9	3.13	0.003
Hsd3b4	Q61767	3 beta-hydroxysteroid dehydrogenase type 4	9	2.99	0.028
Dhtkd1	A2ATU0	Probable 2-oxoglutarate dehydrogenase E1 component DHKTD1, mitochondrial	7	2.93	0.017
Taco1	Q8K0Z7	Translational activator of cytochrome c oxidase 1	2	2.64	0.045
Aif1l	Q9EQX4	Allograft inflammatory factor 1-like	3	2.31	0.001
Gstt2	Q61133	Glutathione S-transferase theta-2	4	2.24	0.002
Sorbs1	Q62417	Sorbin and SH3 domain-containing protein 1	18	2.21	0.036
Tns2	Q8CGB6	Tensin-2	12	2.20	0.007
Farp1	F8VPU2	FERM, RhoGEF and pleckstrin domain-containing protein 1	7	2.13	0.040
Tjp3	Q9QXY1	Tight junction protein ZO-3	7	2.12	0.043
Slc25a42	Q8R0Y8	Mitochondrial coenzyme A transporter SLC25A42	9	1.98	0.021
Mybbp1a	Q7TPV4	Myb-binding protein 1A	13	1.92	0.037
Acnat1	A2AKK5	Acyl-coenzyme A amino acid N-acyltransferase 1	4	1.81	0.046
Epb41l1	Q9Z2H5	Band 4.1-like protein 1	8	1.79	0.023
Col1a1	P11087	Collagen alpha-1(I) chain	8	1.73	0.002
Col4a2	P08122	Collagen alpha-2(IV) chain;Canstatin	5	1.69	0.006
Nomo1	Q6GQT9	Nodal modulator 1	17	1.68	0.014
Col1a2	Q01149	Collagen alpha-2(I) chain	10	1.65	0.001
Dao	P18894	D-amino-acid oxidase	11	1.63	0.002
Arpc4	P59999	Actin-related protein 2/3 complex subunit 4	2	1.62	0.007
Uqcrh	P99028	Cytochrome b-c1 complex subunit 6, mitochondrial	2	1.61	0.019
Atp5l	Q9CPQ8	ATP synthase subunit g, mitochondrial	4	1.59	0.002
Patj	Q63ZW7	Pals1-associated tight junction protein / InaD-like protein	6	1.53	0.003
Dhrs1	Q99L04	Dehydrogenase/reductase SDR family member 1	8	1.53	0.0003
Apmap	Q9D7N9	Adipocyte plasma membrane-associated protein	14	1.52	0.003
Lad1	P57016	Ladinin-1	14	1.49	0.012
Rtn4	Q99P72	Reticulon-4	8	1.49	0.012
F11r	O88792	Junctional adhesion molecule A	2	0.70	0.050

Supplemental Table III. Proteomic profiling of cohort 2, 8-10 week old *Nphs2*^{BioID2}male mice, identifies 50 significantly detected podocyte foot process proteins. MS analysis of *Nphs2*$^{BioID2/+}$ biotin administered mice identifies Kirrel, Tjp, Pard3, Ddn, and Magi as the top 5 proteins detected respectively, with Podocin detected in the top 10. Table list 50 significant proteins ($p \leq 0.05$) at a Log_2 cut off ≥ 1.49 with respective *p*-values in the far-right column. One additional immunoglobulin domain containing protein, Junction adhesion molecule 1 (Jam1 / F11r) was also identified within this MS analysis with a Log_2 fold change of 0.7, $p \leq 0.05$. All proteins were detected with at least two razor unique peptide sequences to the specific protein identified.

Supplemental Table IV.

Gene Symbol	Majority Protein IDs	Protein Names	Razor + Unique Peptides	Log_2 Fold Change	*p* - Value
Kirrel	Q80W68	Kin of IRRE-like protein 1	18	5.99	0.027
Cttn	Q60598	Src substrate cortactin	14	5.70	0.034
Tjp1	P39447	Tight junction protein ZO-1	90	5.62	0.050
Pard3b	Q9CSB4	Partitioning defective 3 homolog B	38	4.21	0.050
Nebl	Q9DC07	LIM zinc-binding domain-containing Nebulette	7	3.41	0.051
Fnbp1l	Q8K012	Formin-binding protein 1-like	7	3.22	0.025
Magi2	Q9WVQ1	Membrane-associated guanylate kinase, WW and PDZ domain-containing protein 2	30	2.89	0.044
Synpo	Q8CC35	Synaptopodin	10	2.88	0.044
Ildr2	B5TVM2	Immunoglobulin-like domain-containing receptor 2	11	2.76	0.003
Tjp2	Q9Z0U1	Tight junction protein ZO-2	21	2.71	0.037
Col1a2	Q01149	Collagen alpha-2(I) chain	3	2.68	0.046
Nphs2	Q91X05	Podocin	13	2.42	0.035
Col1a1	P11087	Collagen alpha-1(I) chain	5	2.37	0.011
Ddn	Q80TS7	Dendrin	13	2.35	0.021
Pkp4	Q68FH0	Plakophilin-4	13	2.27	0.033
Cd2ap	Q9JLQ0	CD2-associated protein	3	2.20	0.034
Rdx; Msn	P26043; P26041	Radixin; Moesin	2	1.74	0.015
Afdn	Q9QZQ1	Afadin	2	1.70	0.030
Hspe1	Q64433	10 kDa heat shock protein, mitochondrial	4	1.66	0.036
Aif1l	Q9EQX4	Allograft inflammatory factor 1-like	5	1.42	0.027
Hist1h4a	P62806	Histone H4	9	1.36	0.014
Tns2	Q8CGB6	Tensin-2	3	1.30	0.038
Khk	P97328	Ketohexokinase	2	1.25	0.027
Clic1	Q9Z1Q5	Chloride intracellular channel protein 1	2	1.21	0.027
Hist2h2bb	Q8CGP2;Q8CGP1	Histone H2B type 1	6	1.04	0.049
Acadl	P51174	Long-chain specific acyl-CoA dehydrogenase, mitochondrial	7	1.01	0.025

Supplemental Table IV. Proteomic profiling of cohort 3, 8-10 week old *Nphs2*^{BioID2} female mice, identifies 28 significantly detected podocyte foot process proteins. MS analysis of biotin administered female *Nphs2*$^{BioID2/+}$ mice identifies Kirrel, Cttn, Tjp, Pard3b, and Nebl as the top 5 proteins detected**.** Table list 28 significant proteins ($p \leq 0.05$) at a Log_2 cut off 1.0 with respective *p*-values in the far-right column. Many documented podocytes SD proteins are identified, *i.e.* Podocin, giving indication the podocin-BioID model is successful. All proteins were detected with at least two razor unique peptide sequences to the specific protein identified.

Supplemental Table V.

Gene Symbol	Protein Names	*p*-Value	Log_2 Fold Change
Kirrel	Kin of IRRE-like protein 1	0.0006	7.75
Tjp1	Tight junction protein ZO-1	0.002	7.63
Nphs2	Podocin	0.019	6.70
Pard3b	Partitioning defective 3 homolog B	0.008	6.39
Magi2	Membrane Associated Guanylate Kinase, WW And PDZ Domain Containing 2	0.018	6.29
Cttn	Src substrate cortactin	0.001	5.60
Ddn	Dendrin	0.003	5.56
Nebl	LIM zinc-binding domain-containing Nebulette	0.010	4.93
Ildr2	Immunoglobulin-like domain-containing receptor 2	0.007	4.90
Fnbp1l	Formin-binding protein 1-like	0.014	4.27
Synpo	Synaptopodin	0.047	2.90
Tjp2	Tight junction protein ZO-2	0.014	4.71
Myzap	Myocardial zonula adherens protein	0.009	3.45
Cd2ap	CD2-associated protein	0.020	3.18
Col1a1	Collagen alpha-1(I) chain	0.007	2.05
Aif1l	Allograft inflammatory factor 1-like	0.014	1.86
Tns2	Tensin-2	0.022	1.75
Magi1	Membrane Associated Guanylate Kinase, WW And PDZ Domain Containing 2	0.002	5.89
Khsrp	Far upstream element-binding protein 2	0.014	4.69
Mapre1	Microtubule-associated protein RP/EB family member 1	0.019	4.56
Yes1	Tyrosine-protein kinase Yes	0.015	4.34
Tmem65	Transmembrane protein 65	0.030	4.25
Ap1g1	AP-1 complex subunit gamma-1	0.018	3.85
Erlin2	Erlin-2	0.008	3.44
Epb41l5	Band 4.1-like protein 5	0.003	3.13
S100g	Protein S100-G	0.034	3.06
Capza2	F-actin-capping protein subunit alpha-2	0.014	2.82
Atp6v1e1	V-type proton ATPase subunit E 1	0.039	2.30
Pkp4	Plakophilin-4	0.033	2.27
Canx	Calnexin	0.042	2.26
Sorbs1	Sorbin and SH3 domain-containing protein 1	0.036	2.21
Farp1	FERM, RhoGEF and pleckstrin domain-containing protein 1	0.040	2.13
Tjp3	Tight junction protein ZO-3	0.043	2.12
Mybbp1a	Myb-binding protein 1A	0.037	1.92
Cndp2	Cytosolic non-specific dipeptidase	0.041	1.83
Epb41l1	Band 4.1-like protein 1	0.023	1.79
Pls3	Plastin-3	0.029	1.76
Rdx	Radixin	0.015	1.74
Msn	Moesin	0.015	1.74
Afdn	Afadin	0.021	1.70
Col4a2	Collagen alpha-2(IV) chain;Canstatin	0.006	1.69
Nomo1	Nodal modulator 1	0.014	1.68
Col1a2	Collagen alpha-2(I) chain	0.0009	1.65
Arpc4	Actin-related protein 2/3 complex subunit 4	0.007	1.62
Sec23a	Protein transport protein Sec23A	0.030	1.59
Patj	Pals 1-associated tight junction protein / InaD-like protein	0.003	1.53
Lad1	Ladinin-1	0.012	1.49
Rtn4	Reticulon-4	0.012	1.49
Cisd2	CDGSH iron-sulfur domain-containing protein 2	0.026	1.46
Naca	Nascent polypeptide-associated complex subunit alpha	0.049	1.46
Scp2	Non-specific lipid-transfer protein	0.026	1.36
Aimp1	Endothelial monocyte-activating polypeptide 2	0.046	1.26
Dhrs7b	Dehydrogenase/reductase SDR family member 7B	0.024	1.24
Clic1	Chloride intracellular channel protein 1	0.027	1.21

274 **Supplemental Table V. Compiled proteomic profile of three cohorts of, 8-10 week old male**
275 **and female, *Nphs2*^{BioID2} mice.** Table list 54 significant proteins ($p \leq 0.05$) at a Log_2 cut off ≥ 1.20,
276 with respective *p*–value listed in the far-right column. Table compiles the proteomic profiles across
277 all three separate analysis and averages their respective Log_2 fold change and *p*-values. This table
278 was subsequently utilized for *Qiagen Ingenuity Pathway Analysis* (IPA) and input into
279 the *Database for Annotation, Visualization, and Integrated Discovery* (DAVID) for gene ontogeny
280 characterization. All proteins were detected with at least 2 razor unique peptides specific to the
281 protein denoted.
282
283
284
285
286
287
288
289
290

Supplemental Figure 1.

A

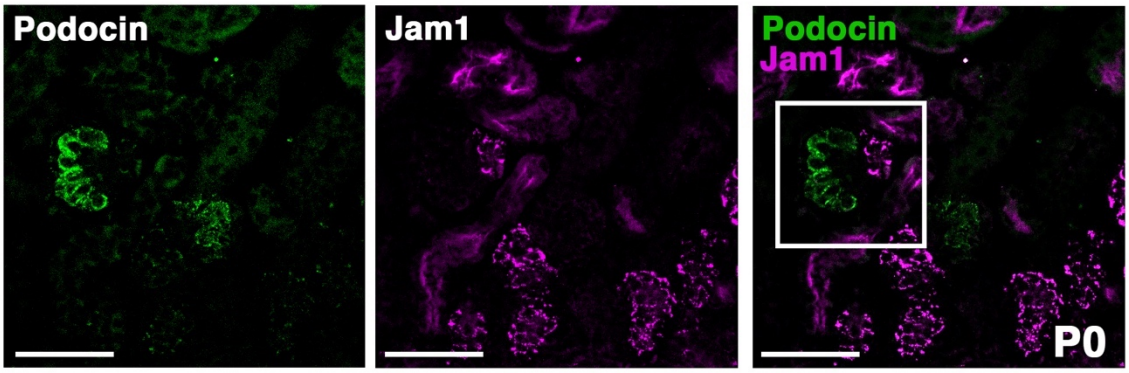

A'

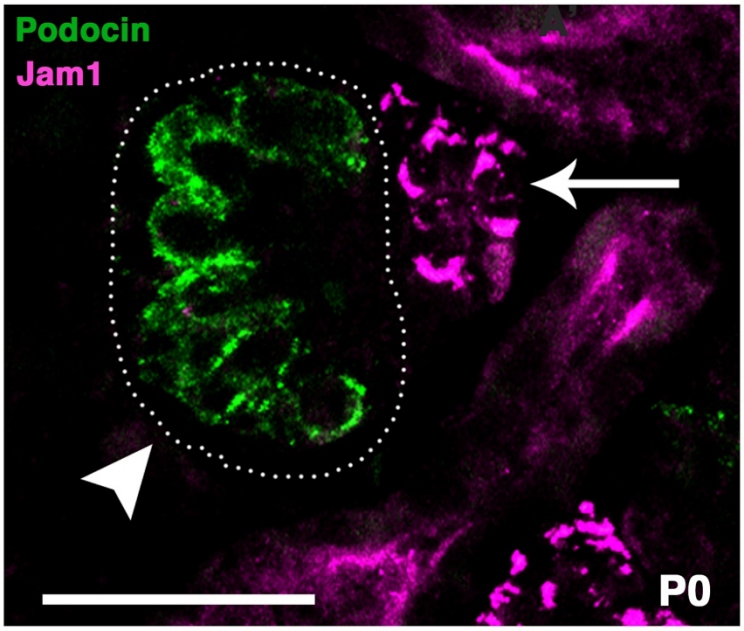

Supplemental Figure 1. Expression of immunoglobulin superfamily member Jam1/F11r in tubule cells neighboring podocytes. (A). Jam1 was identified to have a 0.7 Log_2 fold change in a single mass spec analysis. P0 kidney sections were immunostained for Jam1 (magenta) and podocin (green). Jam1 is localized to tubule cells directly adjacent to podocytes. **(A')** Highlighted white boxed region from **(A)** is enlarged to show podocin localization restricted to the glomerulus, outlined in a dotted while circle, and Jam1 localization in neighboring tubule cells, denoted by white arrow. All scale bars: 50 μm.

323 -

Supplemental Figure 2.

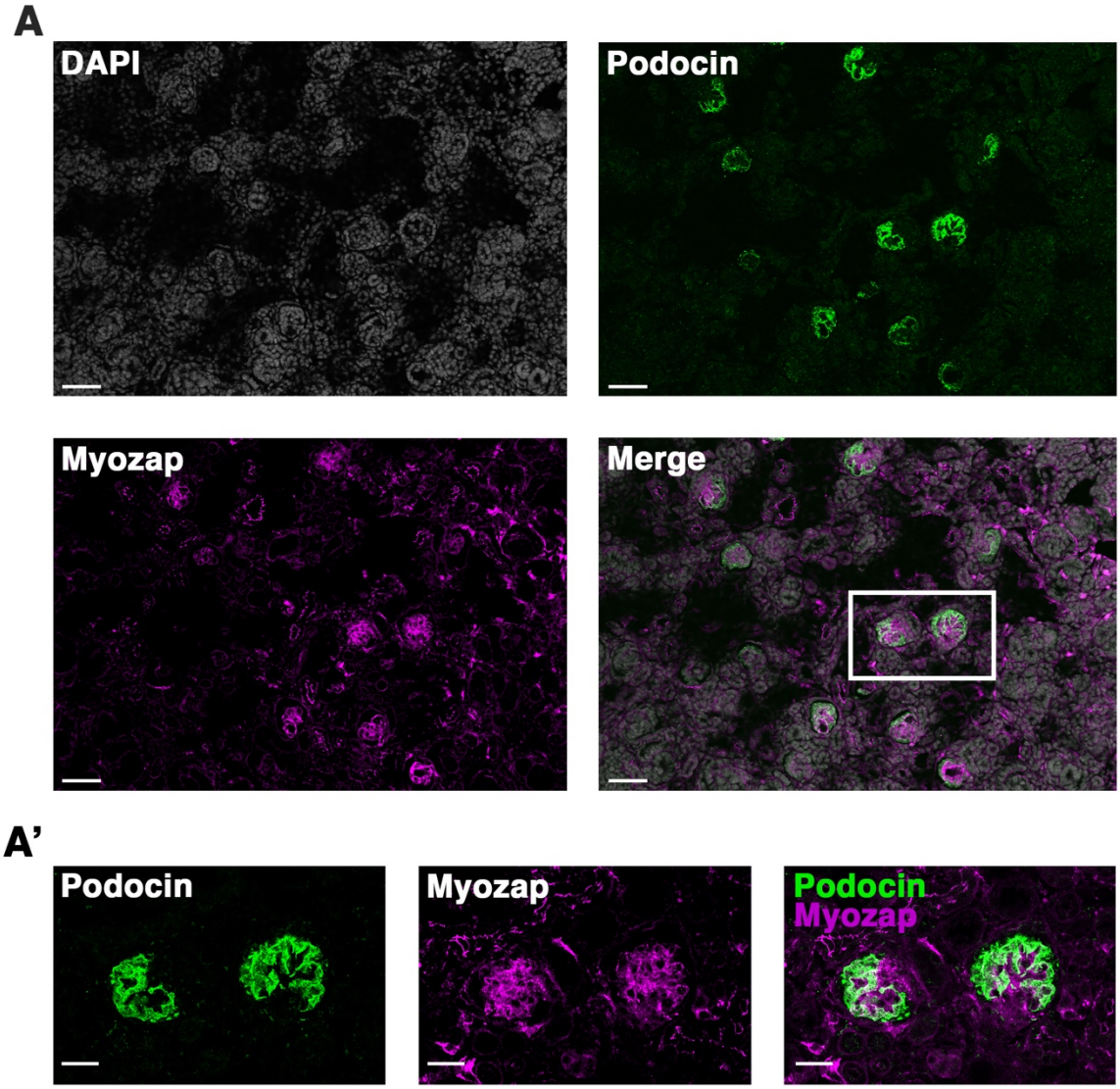

324

Supplemental Figure 2. Myozap localizes to endothelium of glomeruli. (A) Immunofluorescence analysis of Myozap (magenta) identifies strong localization to the central region of the glomerulus and endothelium outside the glomerulus. Proteomic profiling detected a significant Myozap signal (3.45 Log_2 FC), in two of three MS analyses. We observe some overlap (white) between Myozap (magenta) and podocin (green), while the majority of Myozap signal does not overalp with podocin and instead localizes to presumptive endothelium cells. Scale bar: 50 μm **(A')** Highlighted white boxed region from **(A)** indicating staining of Myozap within the endothelium of the glomerulus and some overlap with podocin. Scale bar 20 μm.

Supplemental Figure 3.

A

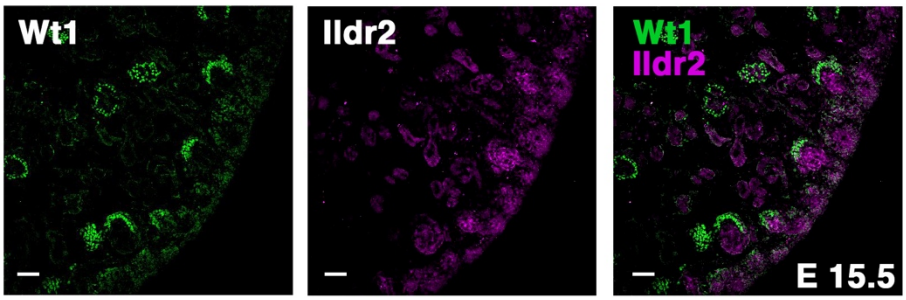

Supplemental Figure 3. Ildr2 is detected in early embryonic nephron precursors including the renal vesicle, comma, and s-shaped bodies. IF analysis of E15.5 animals detects Ildr2 in both continuous membranous staining pattern and in punctate spots. In some S-shaped bodies, denoted by Wt1 expression in developing podocytes (green), Ildr2 (magenta) is detected in a continuous membranous pattern that appears to extend into the tubules, arrow. However, Ildr2 also appears punctate in other renal vesicles, comma, and s-shaped bodies, arrowheads.

Figure 1

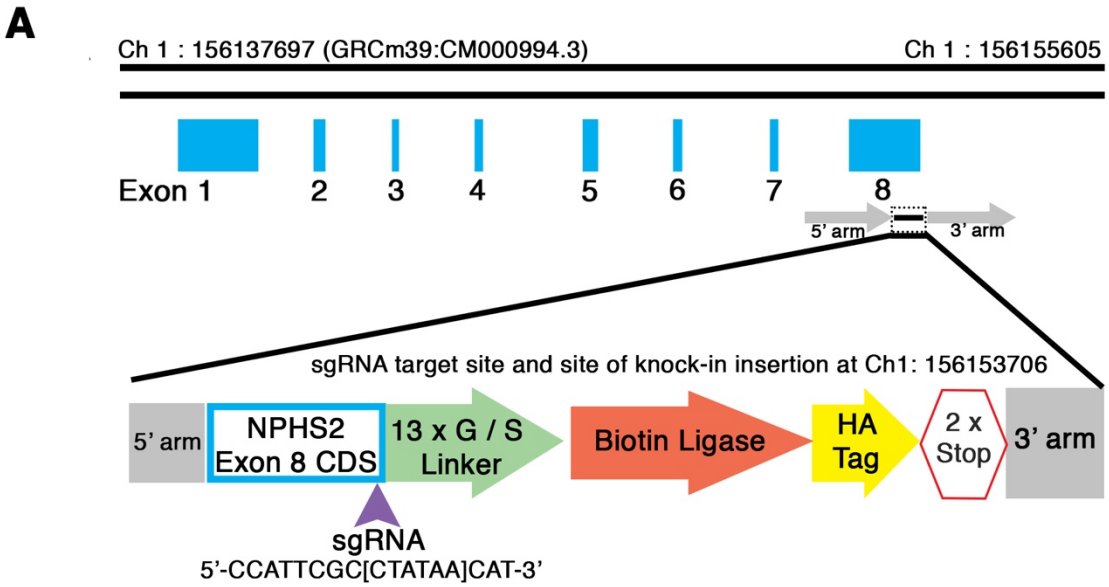

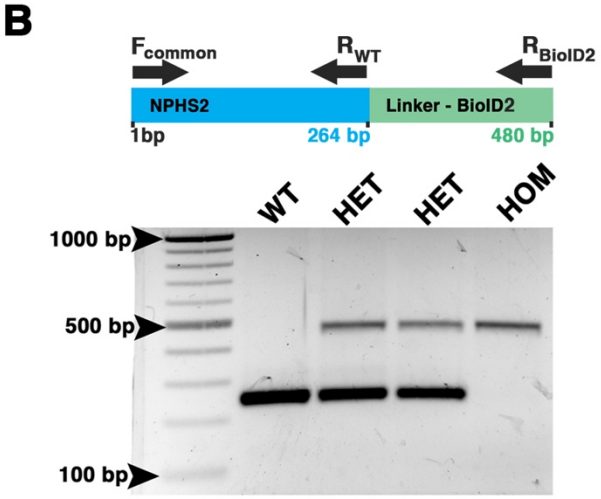

C

Genotype	Number of Embryos	Percentage
WT (+ / +)	21	29
HET(*BioID2* / +)	38	52
HOM (*BioID2* / *BioID2*)	14	19
Total	73	

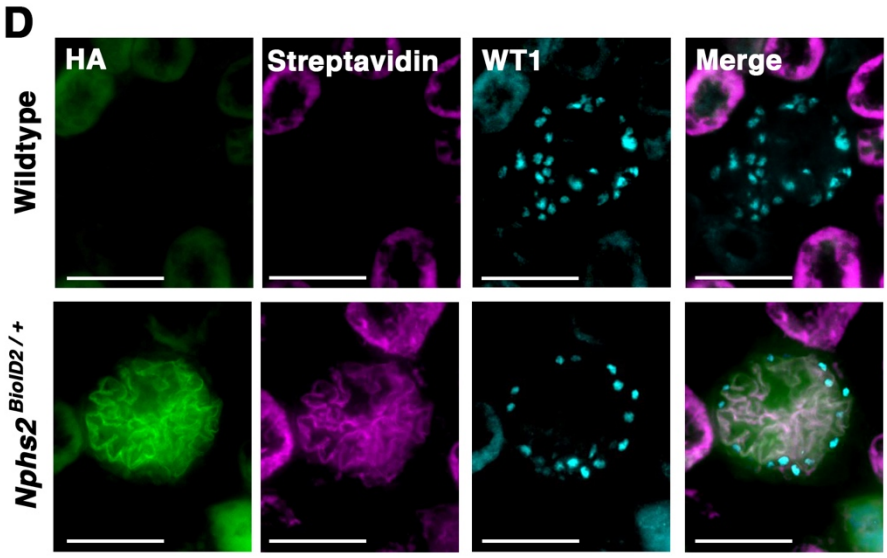

Figure 1. Generation of a knock-in *Nphs2*^{BioID2} mouse line via CRISPR/Cas9 genome editing of the *Nphs2* locus. (A) Schematic of the CRISPR/Cas9 genome editing strategy utilized to generate the *Nphs2*^{BioID2} mouse line. A small guide RNA (sgRNA) targeting the stop codon in exon 8 of *Nphs2* (purple arrowhead) was combined with a donor vector containing the knock-in cassette (zoom view) to induce homologous recombination and integrate the BioID2 moiety containing a 13x Glycine/Serine (G/S) linker, biotin ligase, and HA tag into the *Nphs2* locus. **(B)** Genotyping strategy (top panel) to identify genotype of mice as wildtype (single band at 264 base pairs (bp)), heterozygous (two bands; one at wildtype size of 264 bp and a second that amplifies the BioID2 linker region giving a band at 480 bp), or homozygous (single band at the 480 bp). **(C)** Genotyping of 73 embryos at E18.5-P0, verify an approximate Mendelian ratio of genotypes being recovered (25:50:25). **(D)** IF analysis of 8–10-week-old adult mice injected with biotin illustrate an enrichment of streptavidin detected within the glomerulus of Nphs2^{BioID2} mice and absence of streptavidin signal in control age matched C57BL/6J littermate mice. The HA signal from the BioID2 moiety closely overlaps with streptavidin, observed as white overlap in the merged image. Wilms Tumor (WT1) is utilized as a podocyte marker to delineate the glomerular boundaries. Scale bar: 50 μm

Figure 2.

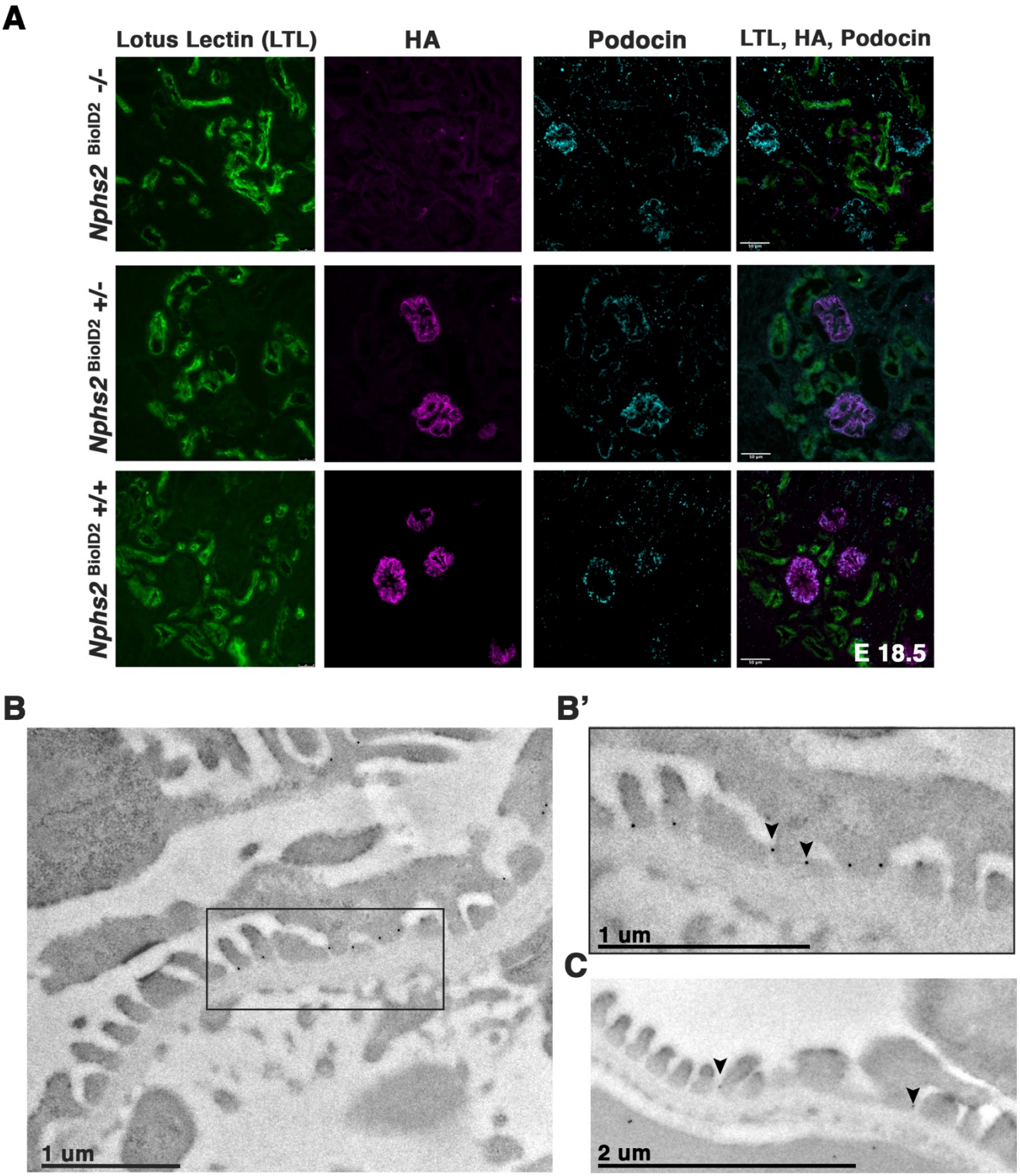
A
Lotus Lectin (LTL)
HA
Podocin
LTL, HA, Podocin
Nphs2 BioID2 -/-
Nphs2 BioID2 +/-
Nphs2 BioID2 +/+
E 18.5
B
1 um
B'
1 um
C
2 um

Figure 2. *Nphs2*^{BioID2} animals present normal kidney morphology with podocin-BioID localized to podocytes and specifically the slit diaphragm. (A) E18.5 littermates of wildtype, heterozygous (*Nphs2*$^{BioID2/+}$), and homozygous (*Nphs2*$^{BioID2/BioID2}$) animals were analyzed for gross kidney morphology and localization of podocin-BioID. The proximal tubule marker lotus lectin (LTL, green) show normal tubule architecture without observation of nephron tubule dilation in heterozygous (*Nphs2*$^{BioID\ /+}$), and homozygous (*Nphs2*$^{BioID2\ /\ BioID2}$) animals. The HA tag (magenta) which is part of the BioID2 moiety was observed to tightly overlap with podocin (cyan) specifically in the glomerulus. The relative size and number of glomeruli was unchanged between control, heterozygous, and homozygous animals. Further, the HA signal was not identified outside of the glomeruli. Scale bar 50 μm **(B)** *Nphs2*$^{BioID2/+}$ localizes to the podocyte slit diaphragm. Utilizing transmission electron microscopy (TEM) and immunogold labeling of 4-week-old murine kidney samples, we detect the anti-HA signal as punctate dots strung just above the GBM adjacent to the podocyte foot process within electron dense regions where the slit diaphragm bridges neighboring foot processes. **(B')** Magnified view of boxed region from panel (B) depicting podocyte foot processes and the electron dense regions between them where the HA signal localizes as dark spherical dots from immunogold labeling, denoted with arrowheads. Scale bar 1 μm **(C)** Wildtype littermates were immunogold labeled for podocin and similarly display localization of podocin at electron dense regions between podocyte foot processes, highlighted with arrowheads. Scale bar 2 μm.

Figure 3

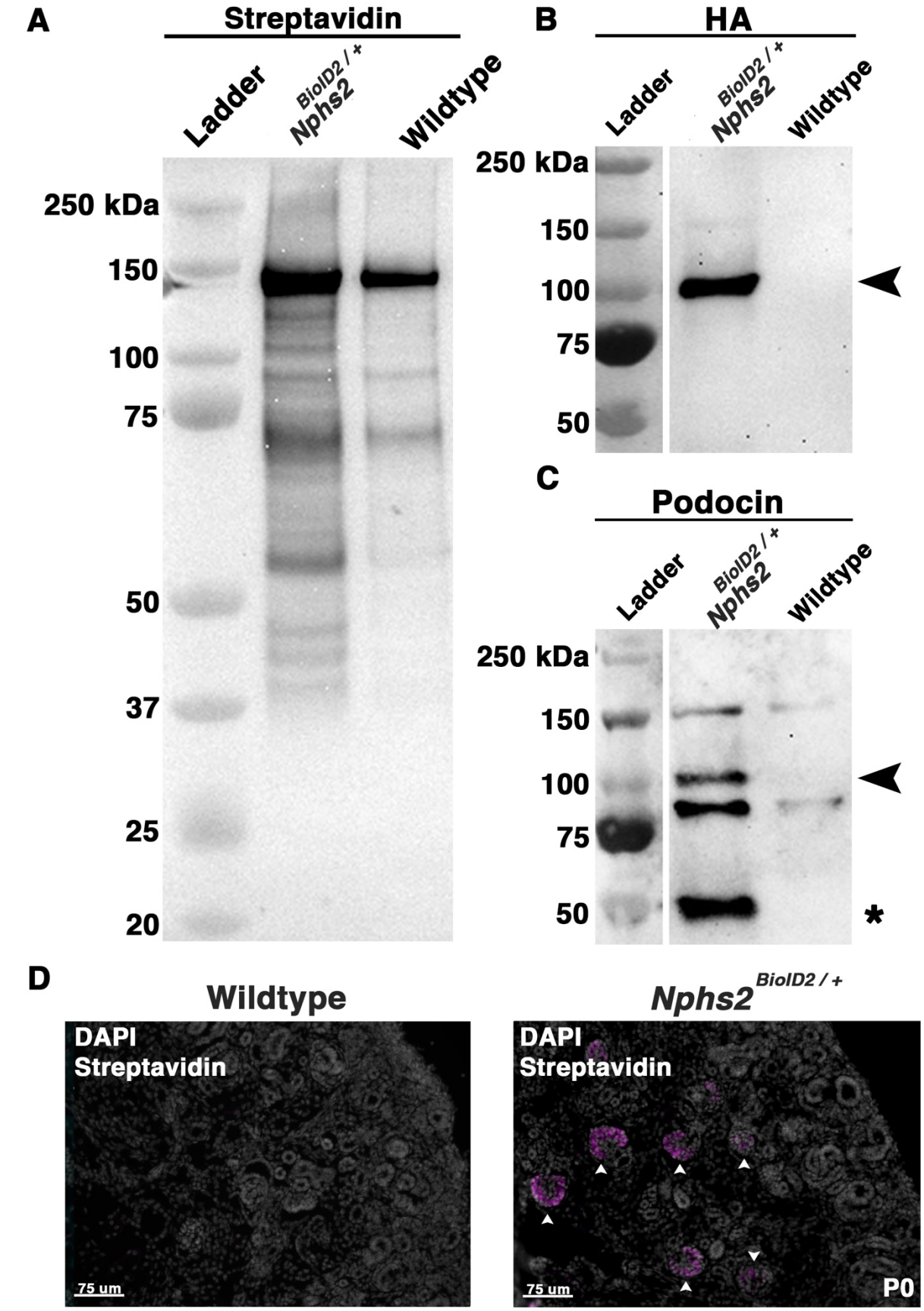

70
71

Figure 3. Biotin administered *Nphs2*$^{BioID2/+}$ mice present an enrichment of biotinylated proteins specifically within glomeruli. (A) A significant enrichment of streptavidin labeled, biotinylated, proteins are observed across the entire molecular weight spectrum in *Nphs2*$^{BioID2/+}$ protein lysates compared to wildtype control littermates, injected with biotin. Streptavidin bead purified lysates were subjected to protein separation and probed for streptavidin. Wildtype age matched, 8–10-week-old, littermate controls present few streptavidin conjugated bands, presumably endogenous metabolic carboxylases. However, *Nphs2*$^{BioID2/+}$ lysates exhibit numerous specific biotinylated protein bands across the entire molecular weight spectrum. **(B)** *Nphs2*$^{BioID/+}$ lysates blotted with an anti-HA antibody present robust and specific detection of the HA signal only within the *Nphs2*$^{BioID2/+}$ sample, indicative of lysate purity. The HA signal is evident at approximately 100 kDa (arrowhead) in *Nphs2*$^{BioID2/+}$ lysates. **(C)** *Nphs2*$^{BioID2/+}$ samples probed for podocin show two specific bands for both BioID2-tagged podocin and endogenous podocin. Adult 8-10-week-old *Nphs2*$^{BioID2/+}$ mice blotted for podocin present a 50kDa band for the endogenous unmodified podocin protein, marked with an asterisk (*) and a second larger band at approximately 100 kDa for the HA tagged podocin-BioID of *Nphs2*$^{BioID2/+}$ mice (arrowhead). **(D)** P0 pups collected from pregnant dams injected with 5 mg/kg of biotin every day from E11.5 to E18.5, and without injection of newborn pups, manifest strong streptavidin detection within glomeruli. Immunofluorescence analysis reveals an enrichment of streptavidin signal (magenta) specifically within the glomeruli (arrowheads) of *Nphs2*$^{BioID2/+}$ kidneys compared to wildtype. Scale bar 75 μm.

Figure 4.

A

Gene Symbol	Protein Names	*p*-Value	Log_2 Fold Change
Kirrel	Kin of IRRE-like protein 1	0.0006	7.75
Tjp1	Tight junction protein ZO-1	0.002	7.63
Nphs2	Podocin	0.019	6.70
Pard3b	Partitioning defective 3 homolog B	0.008	6.39
Magi2	Membrane-associated guanylate kinase, WW and PDZ domain-containing protein 2	0.018	6.29
Cttn	Src substrate cortactin	0.001	5.60
Ddn	Dendrin	0.003	5.56
Nebl	LIM zinc-binding domain-containing Nebulette	0.010	4.93
Ildr2	Immunoglobulin-like domain-containing receptor 2	0.007	4.90
Fnbp1l	Formin-binding protein 1-like	0.014	4.27
Synpo	Synaptopodin	0.047	2.90
Tjp2	Tight junction protein ZO-2	0.014	4.71
Myzap	Myocardial zonula adherens protein	0.009	3.45
Cd2ap	CD2-associated protein	0.020	3.18
Col1a1	Collagen alpha-1(I) chain	0.007	2.05
Aif1l	Allograft inflammatory factor 1-like	0.014	1.86
Tns2	Tensin-2	0.022	1.75

B

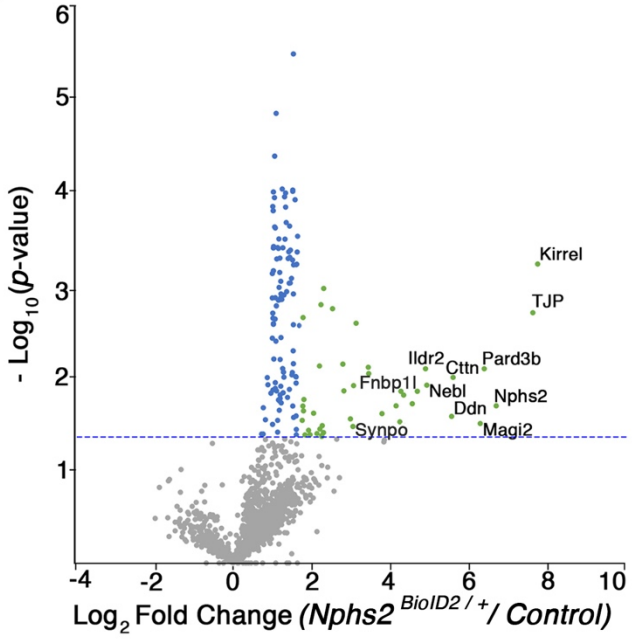

C

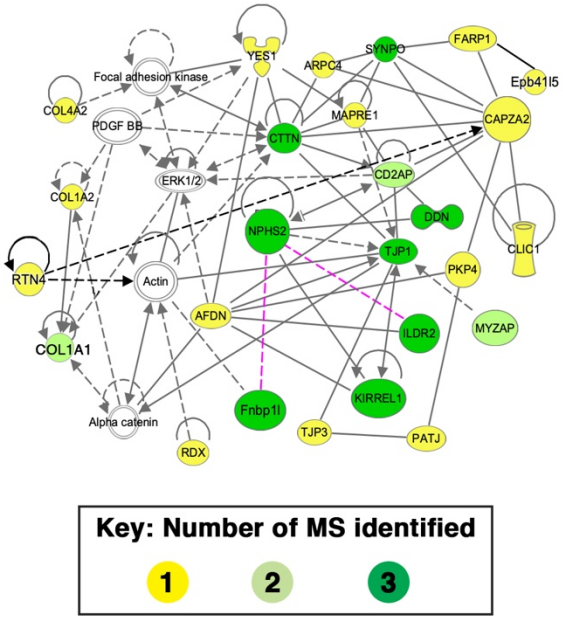

D

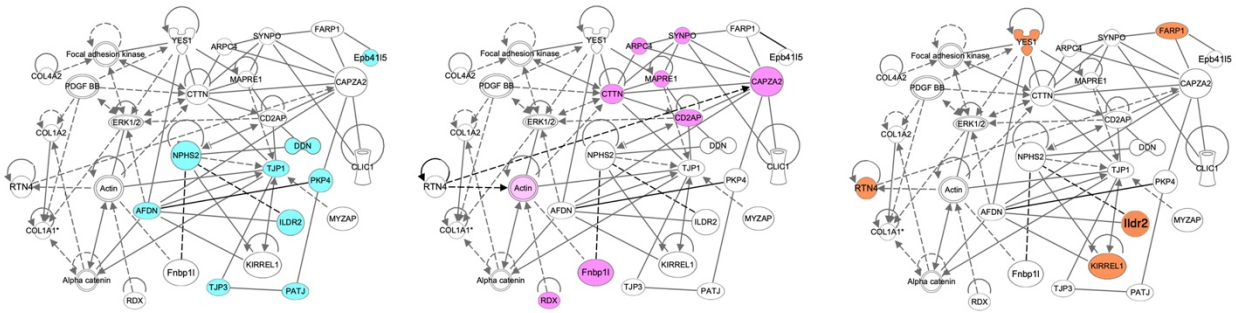

Figure 4. Proteomics profiling of the podocyte foot process identifies documented slit diaphragm components and novel candidates with unexplored podocyte function. (A) Three separate MS analyses were combined, and the average Log_2 fold change and respective *p*-values were averaged to produce a list of the top foot process proteins. The top 11 proteins were identified across all three MS profiles. Six additional proteins were identified across two of the three MS analyses, denoted following the thick black bar. Podocin was a top protein identified and known to oligomerize, indicating our MS proteomic profiling was effective. Additionally, many of the top proteins uncovered, *i.e.*, Kirrel, Dnd, Tjp1/2, Magi2, Pard3, Synpo, and Cd2ap are documented podocyte slit diaphragm components. **(B)** A volcano plot depicting approximately 1400 proteins identified across all three MS analyses. Green dots represent the 40 proteins identified across three separate MS profiles as having a Log_2 fold change ≥ 1.7, and *p*-value ≤ 0.05, blue dots denote all proteins identified to have a significant *p*-value ≤ 0.05, and grey dots are proteins with a *p*-value ≥ 0.05. The top 11 proteins consistently uncovered across all MS analyses are embedded with gene symbols in the plot. The blue dotted line represents a *p*-value ≤ 0.05. **(C)** Network topology was generated utilizing *Qiagen Ingenuity Pathway Analysis* (IPA) on the top 54 proteins from our cumulative proteomic profiles. IPA produces a proposed web of relationships from published literature with most of our top proteins represented, (11 of 17), with documented connections to other foot process and slit diaphragm components. The color intensities of each protein (yellow to green) represent the number of MS analyses from which each protein was identified. Darkest green shade=all three MS analyses, lighter green shade=two of three MS analyses, and yellow=a single MS analysis. Dotted lines and unshaded proteins represent predicted interactions / interactors from IPA analysis, respectively. Magenta lines are novel proteins identified in this study to be present within the podocyte foot process. **(D)** Dissecting the IPA network, identifies three central nodes representing junctions, cytoskeleton, and signaling. Each respective node is color coded with junctions in cyan, cytoskeleton in magenta, and signaling in orange. These computational network topologies and nodes tightly align with podocyte structure and function.

Figure 5.

A

Gene Ontology (GO) Category	Cluster	Enrichment Score	Counts	*p*-Value
Molecular Function (MF)	Cytoskeletal Protein Binding	4.53	12	2.20×10^{-7}
	Actin Binding		6	7.80×10^{-5}
Cellular Component (CC)	Cell-Cell Junction	4.42	12	7.70×10^{-8}
	Adherens Junction		10	7.90×10^{-6}
Biological Process (BP)	Cytoskeleton Organization	2.61	14	3.20×10^{-7}
	Actin Filament-Based Process		12	8.70×10^{-8}

B

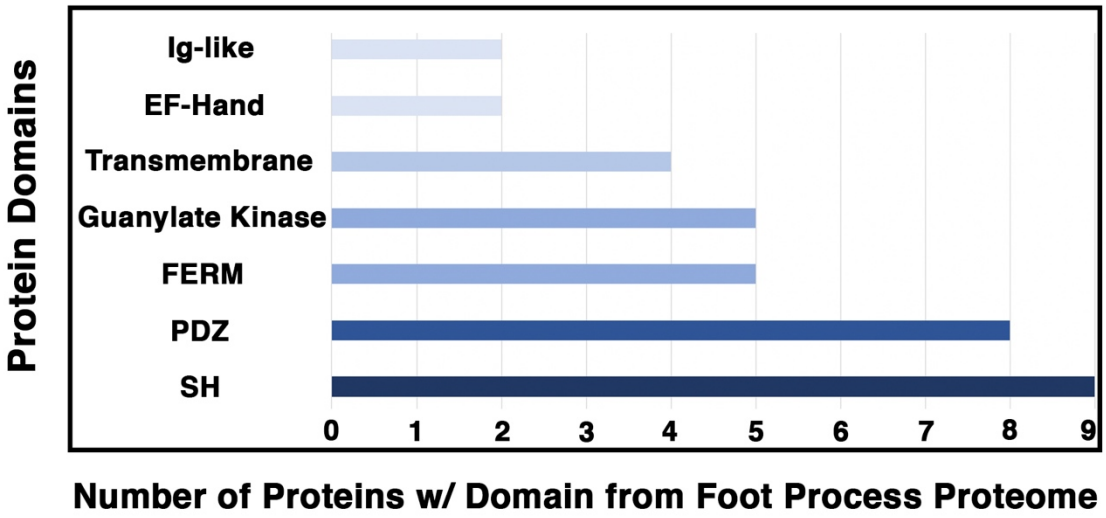

Figure 5. Analysis of the podocyte foot process proteome identifies the cytoskeleton, cell-cell junctions, and actin-based processes as the top GO categories with respective protein domains that align with these functions. The Database for Annotation, Visualization, and Integrative Discovery (DAVID) was utilized for GO clustering analysis of the top 54 proteins identified to have a Log_2 fold change $\geq$ 1.20, and *p*-value $\leq$ 0.05 (Supplemental Table V). **(A)** Overlap in GO readout was observed across the three separate GO categories analyzed, molecular function, cellular component, and biological process, with cytoskeleton, actin, and cellular junctions being the top hits. The respective top clusters within each GO category are listed, alongside the relative enrichment score, number of proteins, and *p*-values. **(B)** Protein domain analysis of the top 54 podocyte foot process proteins provides evidence for protein-protein interactions and likely scaffold and protein-protein complex formation. Each protein's respective protein domains were binary counted for presence or absence within the proteomics profile. The top seven protein domains identified from the podocyte foot process proteome consist of a Src homology (SH) (n = 9 proteins), PSD-95, Disc large, and ZO – 1 (PDZ) (n = 8), 4.1 protein, Ezrin, Radixin and Moesin (FERM) (n = 5), Guanylate Kinase (n = 5), Transmembrane (n = 4), E and F helix – Hand (EF – Hand) (n = 2), and an Immunoglobulin - like (Ig – like) domain (n = 2). Cumulatively, these 7 domains represent ~ 50 % of the top proteins identified from the foot process proteome (26 / 54).

Figure 6.

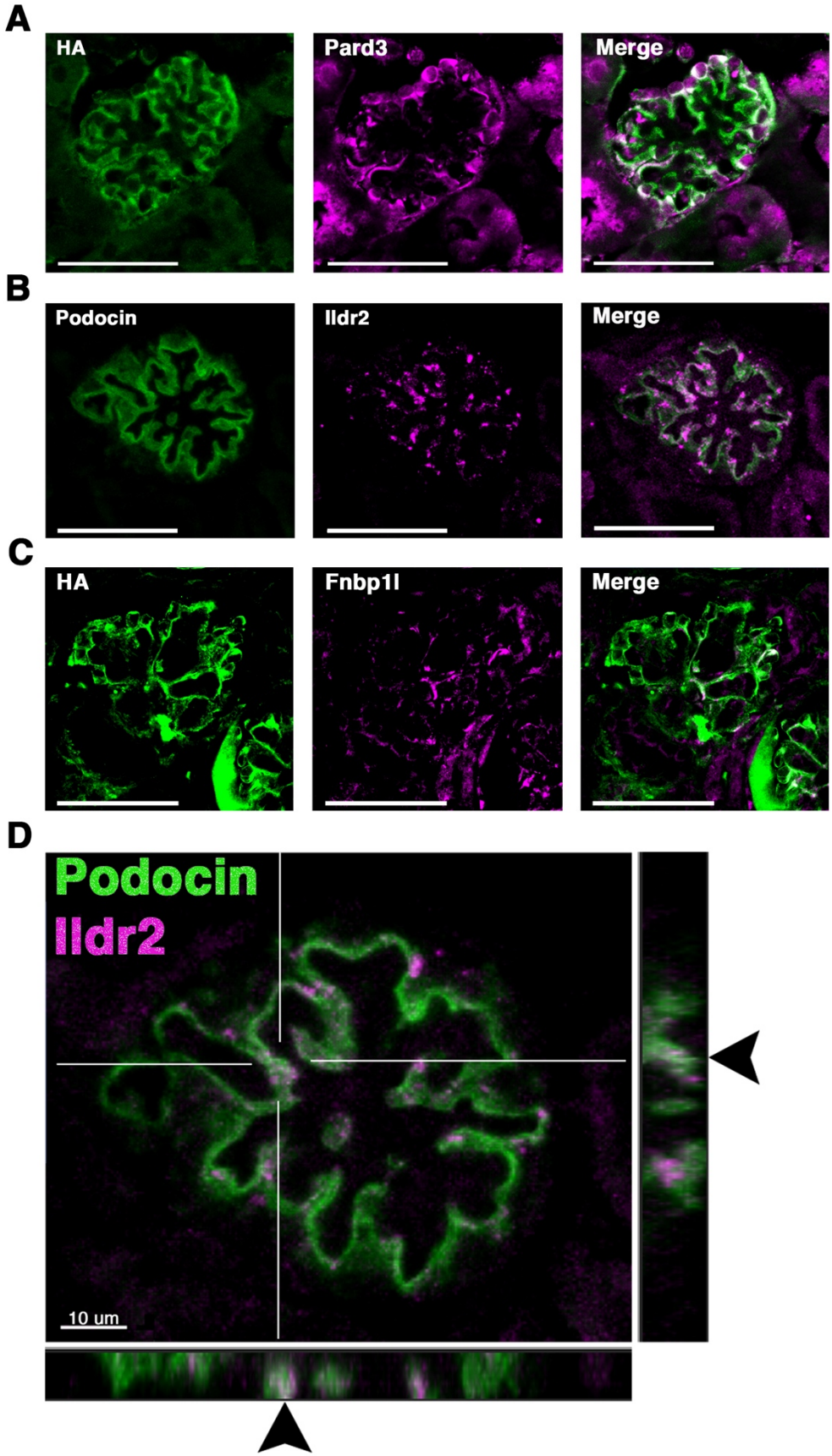
A
HA
Pard3
Merge
B
Podocin
Ildr2
Merge
C
HA
Fnbp1l
Merge
D
Podocin
Ildr2
10 um

154 **Figure 6. Two novel foot process candidates, Ildr2 and Fnbp1l, localize to podocytes and**
155 **overlap with podocin in the foot process.** IF analysis of three top candidates identified from the
156 proteomics profiling, Pard3, Ildr2, and Fnbp1l, were detected within glomeruli. **(A)** Pard3
157 (magenta), a known component of the podocyte foot process, co-localizes with HA signal of
158 podocin-BioID (green) producing a white signal in overlap. **(B)** Ildr2 (magenta) displays a punctate
159 localization pattern within the glomerulus and overlaps (white) with podocin (green). **(C)** Fnbp1l
160 (magenta) co-localizes (white) with HA signal of podocin-BioID (green) in podocytes. Scale bars in
161 A-C: 50 μm **(D)** A merged image of podocin and Ildr2 through a confocal z-projection identifies
162 punctate localization and overlap (white, arrowheads) between podocin (green) and Ildr2
163 (magenta) visualized in the z-plane in the left and bottom panels. Scale bar in D 10 μm.
164

Figure 7.

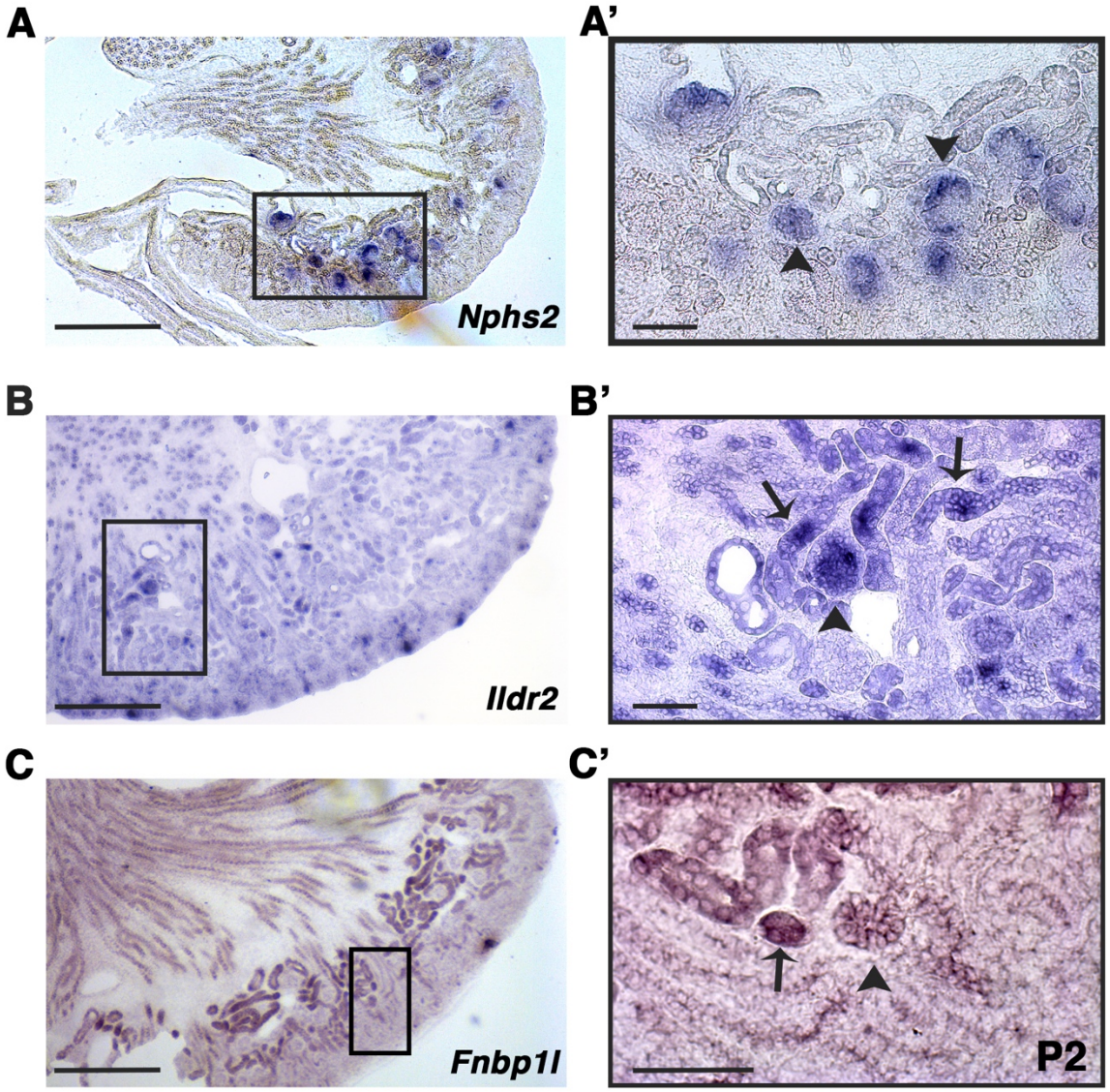

Figure 7. *In situ* hybridization confirms glomerular and some tubule cell expression of *Ildr2* and *Fnbp1l* in P2 kidneys. P2 kidney sections were hybridized with antisense riboprobes against *Nphs2* (podocin)**,** *Ildr2***,** and *Fnbp1l*. **(A)** *Nphs2* (purple) displays strong expression specifically in glomeruli at P2. The rectangular box in **(A)** is enlarged in **(A')** to highlight expression of *Nphs2* only in glomeruli, arrowheads denote example glomeruli **(B)** *Ildr2* transcripts (purple) are identified within glomeruli and tubules. The rectangular box in **(B)** is enlarged in **(B')** to denote expression of *Ildr2* in glomeruli, arrowhead, and in some tubules, black arrow. **(C)** *Fnbp1l* (purple) is identified in both glomeruli and tubules. The block rectangular box in **(C)** is enlarged in **(C')** to denote expression of *Fnbp1l* in glomeruli, arrowhead, and tubules, arrow. Scale bars in A–C: 500 μm. Scale bars in A'-C': 100 μm.

Figure 8.

A

Gene Symbol	Protein Names	BioID (Young) vs WT Log_2 Fold Change	BioID (Aged) vs WT Log_2 Fold Change	*p*-Value
Ildr2	Immunoglobulin-like domain-containing receptor 2	2.76	3.53	0.001
Tjp2	Tight junction protein ZO-2	2.71	3.31	0.01
Pkp4	Plakophilin-4	2.27	2.94	0.01
Nphs2	Podocin	2.42	2.36	0.10
Fnbp1l	Formin-binding protein 1-like	3.22	2.12	0.10
Tns2	Tensin-2	1.30	0.36	0.10

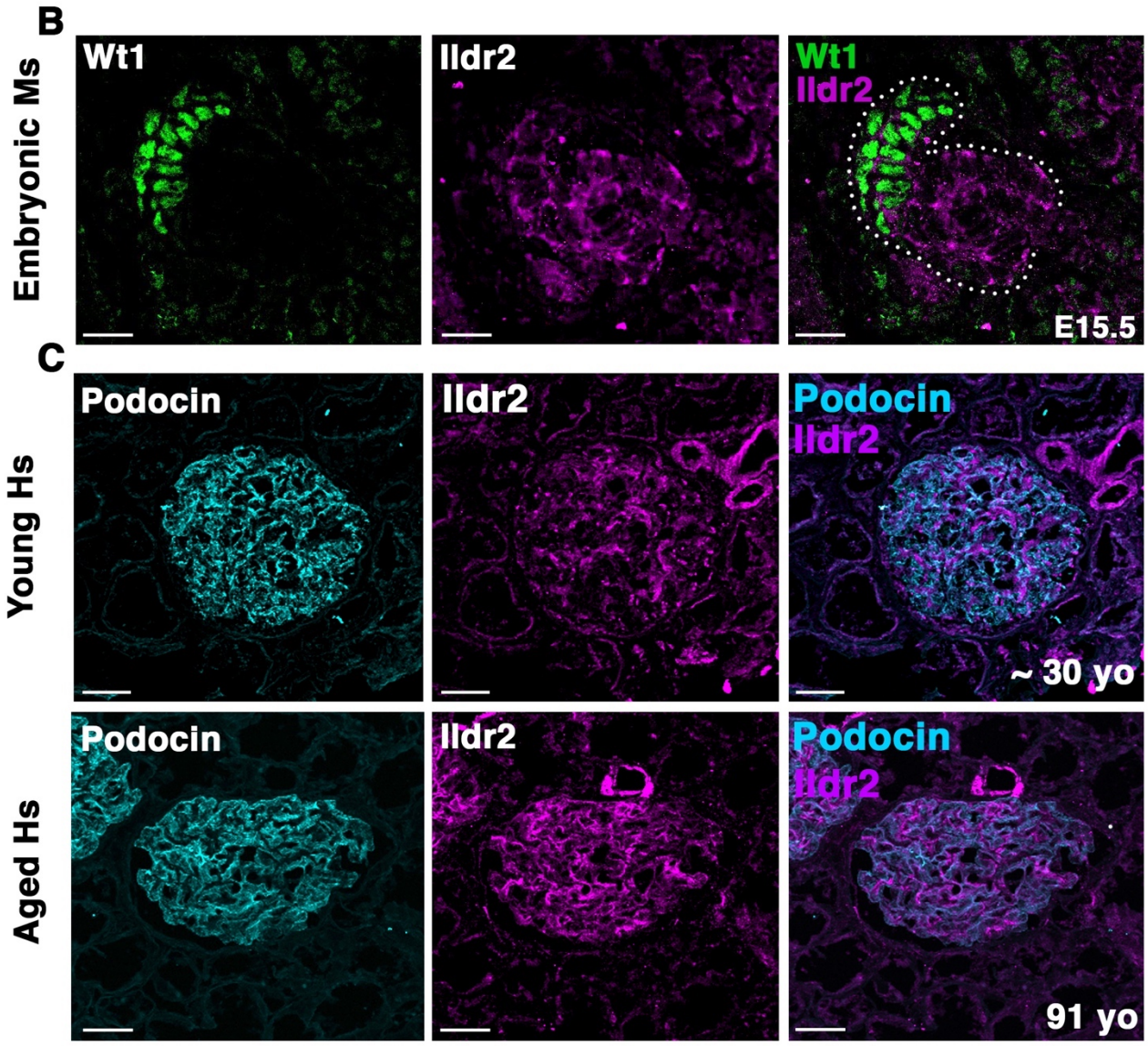

Figure 8. Ildr2 is detected in developing nephron structures and presents increased detection in aged mouse and human glomeruli compared to young. (A) Proteomic profiling of two aged (108 week old) male *Nphs2*$^{BioID2/+}$ mice identifies a significant increase in Ildr2, Tjp2, and Pkp4 protein levels compared to 8-10 week old *Nphs2*$^{BioID2/+}$ mice**.** Table lists 6 proteins with relative detection in "young" 8-10 week old *Nphs2*$^{BioID2/+}$ male mice vs "aged" 108 week old *Nphs2*$^{BioID2/+}$ male mice. All protiens were detected with at least 2 razor unique peptides with their respective *p*-values in far right column. **(B)** Ildr2 is expressed in early developing nephron structures including the renal vesicle, comma, and s-shaped bodies with podocytes denoted by the Wt1-positive nuclei. Ildr2 (magenta) is observed as membranous along the comma / s-shapped body with some punctate foci in E15.5 mouse kidney cortex, outlined with white dots. Scale bar: 20 μm**. (C)** Young and aged (91 yo) human kidney tissue was probed of Ildr2 via IF. Young human glomeruli display punctate foci detection of Ildr2 (magenta) similar to 8-10 week old mice. However, aged (91 yo) male glomeruli evince an increase in Ildr2 detection within glomeruli. Furthermore, where Ildr2 looks to be more highly detected in these aged glomeruli podocin appears less detectable. Scale bar: 50 μm.

Figure 9

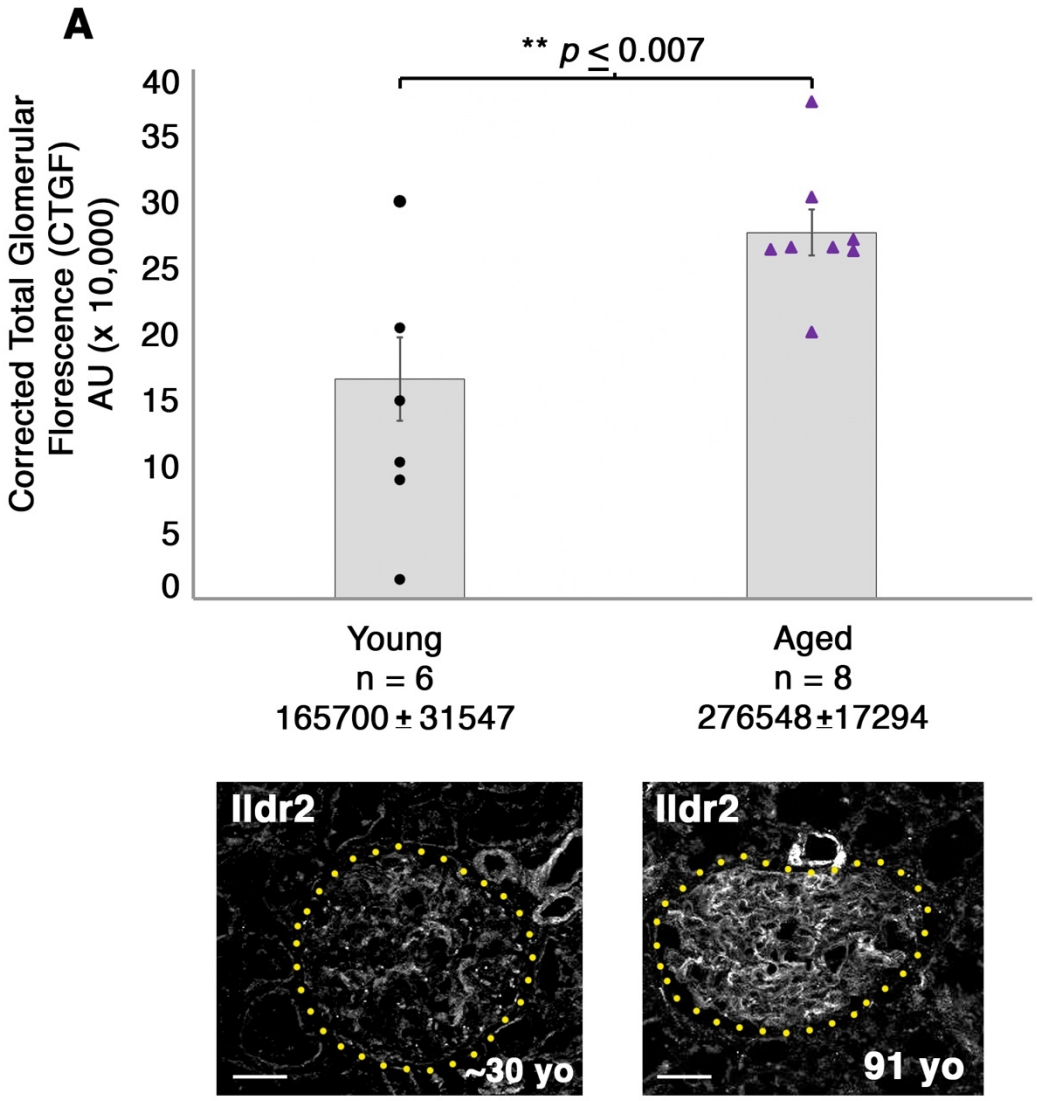
A
** $p \leq 0.007$
Corrected Total Glomerular Florescence (CTGF) AU (x 10,000)
40
35
30
25
20
15
10
5
0
Young
n = 6
165700 ± 31547
Aged
n = 8
276548 ±17294
lldr2
~30 yo
lldr2
91 yo

Figure 9. Aged 91 yo glomeruli exhibit a significant increase in corrected total glomerular florecence (CTGF) compared to young human glomeruli. We observe a significant ($p \leq 0.007$) increase, of approximatly 67%, in CTFG in aged human lldr2 detection compared to young human tissue. CTGF was calculated by selecting the gomeruli as the ROI then measuring the total florescence within the area and subtracting out the sum of the area by the average background florecence, *i.e.* Total gROI florecence – (Area of glomerulus *x* mean of background florescence) = CTGF. Two example glomeruli are displayed and outlined in yellow dots to depict the respective ROI utilized to calculate CTGF. Scale bar: 50 μm.